Updraft Maintenance and Axisymmetrization during Secondary Eyewall Formation in a Model Simulation of Hurricane Matthew (2016)

CHAU-LAM YU,[a] ANTHONY C. DIDLAKE JR.,[b] AND FUQING ZHANG[b,c]

[a] *Department of Atmospheric and Environmental Sciences, University at Albany, State University of New York, Albany, New York*
[b] *Department of Meteorology and Atmospheric Science, The Pennsylvania State University, University Park, Pennsylvania*
[c] *Center for Advanced Data Assimilation and Predictability Techniques, The Pennsylvania State University, University Park, Pennsylvania*

(Manuscript received 16 April 2021, in final form 30 December 2021)

ABSTRACT: As a follow-on to a previous study on secondary eyewall formation (SEF) in a simulation of Hurricane Matthew (2016), this study investigates the emergence and maintenance of an asymmetric rainband updraft region that leads to an SEF event. Under moderate deep-layer environmental wind shear, the storm develops a quasi-stationary rainband complex with intense, persistent updrafts in its left-of-shear, downwind end. Using a budget of equivalent potential temperature θ_E, it is demonstrated that the maintenance of the left-of-shear updraft is aided by a mesoscale cold pool induced by rainband stratiform cooling which interacts with the storm's moist envelope of high-θ_E air. An extended period of destabilization occurs through differential horizontal advection of θ_E in the boundary layer, which continuously replenishes the moist instability that would otherwise be depleted by the updrafts. The initial lifting of the updraft is found to be the result of buoyancy advection resulting from the density contrast between the surface cold pool and the inner-core high-θ_E air. A potential vorticity (PV) budget analysis shows that these left-of-shear updrafts generate low- to midlevel PV through diabatic heating and boundary layer processes, which shapes the local PV enhancement and propagates cyclonically downwind. Meanwhile, in the mid- to upper levels, eddy PV flux convergence and PV generation continue to occur in the stratiform precipitation extending downwind into the upshear quadrants, which substantially increases the azimuthal mean PV at the radius of the developing secondary eyewall and marks the occurrence of the axisymmetrization process.

KEYWORDS: Conditional instability; Rainbands; Updrafts/downdrafts; Stratiform clouds; Tropical cyclones; Data assimilation

1. Introduction

Secondary eyewall formation (SEF) in tropical cyclones (TCs) remains an outstanding problem for TC forecasts despite its frequent occurrence in nature. This is in part due to the lack of a complete scientific understanding of the evolution of TC inner cores. To address this issue, previous work has heavily focused on understanding the fundamental physical processes that underlie SEF (e.g., Huang et al. 2012; Abarca and Montgomery 2013; Qiu and Tan 2013; Zhang et al. 2017; Wang et al. 2019; Wang and Tan 2020) as it is a marked reorganization of the TC inner-core structure and can cause substantial intensity change. The current study continues this investigation in a follow-on to Yu et al. (2021), which examined the connection between the asymmetric and axisymmetric features and processes to understand the evolving tangential wind structure leading into SEF.

Several theories have been proposed for the physical mechanisms for SEF. Some studies focus on axisymmetric SEF dynamics and hypothesize that asymmetric eddy features can contribute to the azimuthal mean TC evolution from a wave–mean-flow interaction perspective. These hypotheses include the stagnation and axisymmetrization of vortex Rossby waves (VRWs) at a critical radius (Montgomery and Kallenbach 1997), the beta-skirt axisymmetrization via an upscale cascade of vorticity perturbations (Terwey and Montgomery 2008), and upscale growth of convective perturbations in a zone of declining rapid filamentation outside the eyewall (Rozoff et al. 2006) and in the outer rainbands (Wang et al. 2019). Other studies also highlighted the role of axisymmetric boundary layer processes during SEF. These include a progressive boundary layer control pathway emphasizing unbalanced boundary layer dynamics (Huang et al. 2012; Abarca and Montgomery 2013, 2014; Abarca et al. 2015) and a steady-state boundary layer response to pressure forcing associated with boundary layer top vorticity anomalies (Kepert 2013; Kepert and Nolan 2014).

A common requirement in these axisymmetric SEF theories is a preexisting axisymmetric vorticity anomaly in the TC outer core to initiate the upscale growth process or the coupling between the troposphere and boundary layer processes (e.g., Miyamoto et al. 2018). Given the importance of this necessary axisymmetric projection, we need to understand the asymmetric processes that are most efficient or common for reaching this critical threshold. Owing to their large spatial coverage, outer rainbands are a potential source for such an axisymmetric vorticity anomaly. Indeed, several other studies have demonstrated that the secondary eyewall is often axisymmetrized from asymmetric outer rainband features (e.g., Qiu and Tan 2013; Wang et al. 2019; Wang and Tan 2020).

Observational and modeling studies have found that the primary organizing factor for TC outer rainbands is deep-layer environmental wind shear (e.g., Hence and Houze 2012;

Zhang: Deceased.

Corresponding author: Chau Lam Yu, cyu7@albany.edu

DOI: 10.1175/JAS-D-21-0103.1

Riemer 2016; Li et al. 2017). Under the asymmetric forcing associated with sufficiently strong shear, TC rainbands tend to form a quasi-stationary, long-lived system, termed the stationary band complex (SBC; Willoughby et al. 1984), that primarily lies in the downshear half of the storm (Hence and Houze 2012). As nascent convective cells are initiated and mature in the downshear-right quadrant (Corbosiero and Molinari 2002, 2003), they propagate to the left-of-shear half of the storm and gradually weaken, collapsing into widespread stratiform precipitation (Didlake and Houze 2013; Riemer 2016).

Despite having less vigorous vertical exchanges than its upwind counterpart, the downwind stratiform rainband may have a critical role in SEF processes (Qiu and Tan 2013; Fang and Zhang 2012; Didlake and Houze 2013; Dai et al. 2017; Zhang et al. 2017; Didlake et al. 2018). Didlake and Houze (2013) found a mesoscale descending inflow (MDI) in the stratiform rainband complex of Hurricane Rita (2005), which extended from the mid- to upper troposphere into the boundary layer. A similar MDI feature was also found in Hurricane Earl (2010), which had a clear robust updraft on the inward side of the MDI that contributed to the subsequent SEF (Didlake et al. 2018). Qiu and Tan (2013) similarly identified a mesoscale, negatively buoyant downdraft within the stratiform rainband that connected to an enhanced boundary layer inflow region, which triggered new convective updrafts along its inner edge. Other modeling studies also showed that latent cooling in stratiform rainbands produce a favorable thermodynamic environment for initiating outer-core convection, and increases the likelihood of SEF (Li et al. 2014; Zhu et al. 2015; Tyner et al. 2018; Chen 2018; Chen et al. 2018). Using idealized, dry simulations, Yu and Didlake (2019) examined the vortex response to prescribed stratiform diabatic forcing and showed that a mesoscale updraft can be triggered on the inward and upwind side of the MDI. Their findings provided a potential explanation for the mechanism and relative placement of these important features commonly observed prior to SEF.

Overall, these studies describe a dynamical connection between an organized rainband complex and SEF, where the downwind stratiform portion sets up a cooling-driven MDI and a surface cold pool that helps to initiate new convective updrafts that are the precursors to the secondary eyewall axisymmetric updraft. Yu et al. (2021) examined this process in an SEF event of a full-physics simulation of Hurricane Matthew (2016) by first focusing on the evolving tangential wind field. Prior to SEF onset, the TC develops a stationary rainband complex and an accompanying storm-scale wind acceleration in the left-of-shear quadrants. This broad wind acceleration is driven by a midlevel irrotational inflow that draws high-angular-momentum air from the environment inward. Induced by stratiform diabatic forcing, this irrotational inflow is collocated with a downdraft, resembling the MDI found in previous observations (Didlake and Houze 2013; Didlake et al. 2018). Along the inner edge of the MDI, intense updrafts are triggered upon interaction with the boundary layer, as consistent with previously mentioned studies. However, the exact mechanism that leads to these intense updrafts and their impact on secondary eyewall formation were not fully investigated. In this study, we examine the dynamics of the emergence and maintenance of the rainband convective updrafts in our simulation of Hurricane Matthew. We emphasize understanding how the downwind rainband processes interact with the boundary layer to result in a low-level thermodynamic structure conducive for triggering and sustaining prolonged updrafts and subsequent diabatic heating. We then perform a potential vorticity analysis to examine how the asymmetric updrafts can substantially increase the azimuthal mean potential vorticity at outer radii, which subsequently leads to the axisymmetrization of the outer eyewall.

The paper is organized as follows: sections 2 and 3 describe the model simulation and budgeting methods used in the study, section 4 examines the role of boundary layer thermodynamics in updraft maintenance and initiation during the SEF period using the moist instability parameter $\partial\theta_E/\partial z$ and Lagrangian analysis, section 5 uses a potential vorticity budget to examine how the asymmetric updrafts lead to the axisymmetrization of the secondary eyewall, and section 6 provides the conclusions of the study.

2. Methodology

a. Model and data

This study examines a high-resolution, convection-permitting, full-physics simulation of Hurricane Matthew during its peak intensity in the Caribbean Sea near 0000 UTC 3 October. The model simulation is the same as in Yu et al. (2021), which uses the Weather Research and Forecasting (WRF) Model v3.5.1 (Skamarock et al. 2008) and consists of four two-way-nested domains (the three inner domains being vortex-following) with horizontal grid spacings of 27, 9, 3, and 1 km. The simulation is initialized with an ensemble Kalman filter (EnKF) analysis mean at 0000 UTC 2 October 2016 from the Pennsylvania State University WRF-EnKF system (e.g., Weng and Zhang 2016; Nystrom et al. 2018); this data assimilation system assimilates all available conventional observations, synthetic hurricane position and intensity observations, airborne Doppler radar super observations (Gamache et al. 1995; Weng and Zhang 2012), and dropsonde observations. The model physics are identical to that in Zhang and Weng (2015), which include the WSM6 microphysics scheme (Hong et al. 2004), and the YSU boundary layer scheme (Noh et al. 2003). More details about the data assimilation procedure, model configurations, and simulation verification can be found in Yu et al. (2021).

b. Budget equations

In this study, we examine budgets of equivalent potential temperature and potential vorticity to understand the rainband updraft mechanisms leading to axisymmetrization and SEF. These budgets are performed in a storm-relative framework using WRF output at 1-min frequency.

1) Equivalent potential temperature

Equivalent potential temperature (θ_E) is an integrated variable that comprises of entropy and latent heat energy, and is

conserved in saturated reversible processes. In this study, the Bolton (1980) approximated formula for θ_E is used:

$$\theta_E = \theta \exp\left[\left(\frac{3.376}{T_L} - 0.00254\right) \times q_v\left(1 + 0.81 \times 10^{-3} q_v\right)\right], \tag{1}$$

where θ is dry potential temperature, q_v is vapor mixing ratio, and T_L is the air parcel temperature at the lifting condensation level. The storm-following θ_E budget is given by

$$\frac{\partial \theta_E}{\partial t} + \mathbf{v} \cdot \nabla_h \theta_E + w \frac{\partial \theta_E}{\partial z} = F_{\theta_E}, \tag{2}$$

where $\partial/\partial t$ is storm-relative local tendency operator; ∇_h is the horizontal gradient operator; $\mathbf{v}$ is the storm-relative horizontal wind; F_{θ_E} is the forcing of θ_E, which is calculated as a residual within the WRF Model. It is found that the structure of the residual forcing agrees well with the Rotunno and Emanuel (1987) analytical forcing expression of θ_E, which verifies the calculation of our θ_E budget. We note that the WRF Model is not designed to precisely conserve the θ_E in Eq. (1), nor is the θ_E as computed by this formulation precisely conserved in the real atmosphere (since phase changes in the atmosphere are not actually pseudoadiabatic). But since the evolution of θ_E contains important information about how energy is converted between latent energy and entropy, its budget can explain the concurrent dynamics of the moist processes.

2) POTENTIAL VORTICITY

Ertel's potential vorticity (PV) is a physical quantity that incorporates the evolution of both the dynamics and thermodynamics of a system, and has been used to understand many fundamental processes of TCs (Schubert and Hack 1983; Hausman et al. 2006; Martinez et al. 2019). The traditional Ertel's PV is conserved in adiabatic, frictionless motion of a dry system. For moist flow, Schubert et al. (2001) showed that the conservation property of PV can be retained by using the "virtual potential temperature"; here, we refer to this variable as the density potential temperature θ_ρ {$\theta_\rho = \theta[(1 + q_v/\varepsilon)/(1 + q_v + q_l + q_i)]$ with θ being the dry potential temperature; q_v, q_l, and q_i the mixing ratio of vapor, liquid, and ice phase hydrometeors; ε the ratio of dry to vapor gas constants}. The resulting storm-relative conservation equation is given by

$$\frac{\partial P}{\partial t} + \mathbf{v} \cdot \nabla_h P + w \frac{\partial P}{\partial z} = \frac{1}{\rho}\left[(\nabla \times \mathbf{F}) \cdot \nabla \theta_\rho + \boldsymbol{\zeta}_a \cdot \nabla \dot{\theta}_\rho + P \nabla \cdot (\rho_r \mathbf{U})\right], \tag{3}$$

where $P = 1/\rho(\boldsymbol{\zeta}_a \cdot \nabla \theta_\rho)$ is the moist PV; ρ is the total mass density; $\boldsymbol{\zeta}_a$ is the absolute vorticity vector; $\dot{\theta}_\rho$ is external forcing for density potential temperature; $\mathbf{F}$ is the frictional force per unit mass; ρ_r is the density of precipitating water substance (liquid or ice); and $\mathbf{U}$ is the air-relative terminal fall velocity of precipitation. The terms on the right-hand side of Eq. (3) are the external forcing of PV due to mechanical forcing, diabatic heating, and precipitation. To complete the budget, external forcings for the three-dimensional wind, potential temperature θ, and water vapor mixing ratio q_v are output from the model to compute the PV forcing.

3. Overview of SEF in the Matthew simulation

Figures 1a and 1b show the azimuthally averaged vertical motion at $z = 1.5$ km and tangential wind at $z = 2.86$ km during the first 36-h simulation period of the storm. Figures 1c and 1d show the mean environmental wind structure and 850–200-hPa shear averaged from hours 15 to 25, and the evolution of the shear direction and magnitude. The details of the shear calculation can be found in Yu et al. (2021). The simulated storm reaches maximum tangential winds of 60 m s^{-1} with a radius of maximum wind of ~10 km by hour 7. During hours 15–16, the wind shear magnitude is steady at a moderate value of ~5 m s^{-1}, which helps form a stationary band complex (SBC) in the downshear quadrants, as seen in the plan views of vertical velocity (Fig. 2). At hour 16, a clear azimuthal mean updraft (Fig. 1a) and a sudden kink in the azimuthal mean tangential wind (Fig. 1b, indicated by the dotted–dashed line) emerges as a result of the SBC near 60-km radius (Figs. 2a,b). These inward contracting azimuthal mean signals mark the beginning of SEF. As in Yu et al. (2021), the timing of a formed secondary eyewall is defined as the hour when all four shear-relative quadrants show a clear secondary maximum of vertical velocity, which occurs at hour 22 in this simulation. Based on this definition of SEF time, we refer to the time period from hours 15 to 22 as the Pre-SEF period, and the sequence after hour 22 as the ERC period (hours 23–25). After hour 22, the inner eyewall starts to decay and is subsequently replaced by the outer eyewall at hour 25, which stabilizes at a larger radius of 20 km.

As seen in Fig. 2, hours 17–19 display SBC updrafts that intensify and gradually shift downwind from the downshear-right (DR) quadrant toward the downshear-left (DL) quadrant. This downwind development along the inward spiraling SBC results in the inward contracting signal of the azimuthal mean updraft shown in Fig. 1a. At hour 20, the SBC updrafts in the DL show a clear extension toward the upshear-left (UL) quadrant. Near hour 21, the left-of-shear portion of the SBC continuously propagates and wraps around the storm (Fig. 2g). At hour 22, the secondary eyewall is formed, displaying a circular updraft ring surrounding the inner eyewall near 25-km radius.

4. Thermodynamic evolution

a. *Thermodynamic structure prior to SEF*

Leading into hour 20, the SBC shows a clear downwind development toward the left-of-shear half of the storm before axisymmetrization begins at hour 21. This indicates that the strong updrafts in the downwind portion of the SBC near hours 19 and 20 may play an important role in the

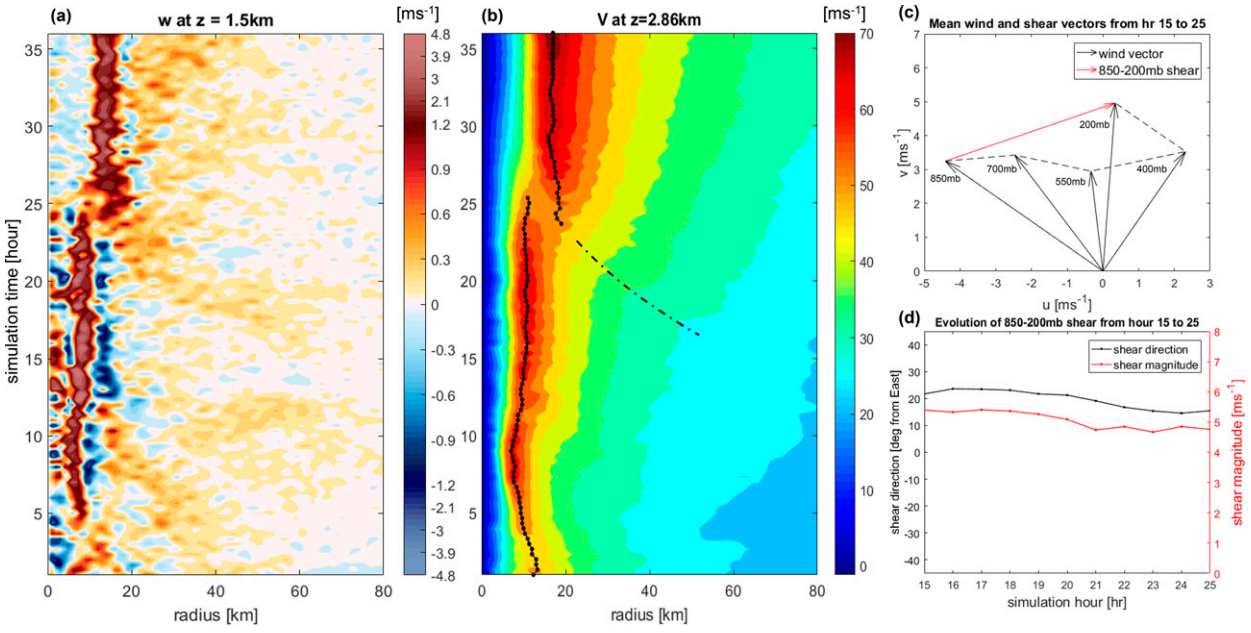

FIG. 1. (a) Hovmöller diagram of the axisymmetric vertical velocity at $z = 1.5$ km. (b) As in (a), but for tangential velocity at $z = 2.86$ km. Black dotted lines indicate radius of maximum wind of the primary and secondary eyewalls. The black dash–dotted line follows the tangential wind increase associated with the inward-contracting updraft signal shown in (a). (c) Hodograph of environmental wind vectors at indicated pressure levels (black) and 850–200-hPa environmental shear vector (red), all averaged over hours 15–25. (d) Time evolution of the 850–200-hPa shear direction (black) and magnitude (red) from hours 15 to 25.

formation process of the secondary eyewall. In this section, we focus on the left-of-shear thermodynamic structures that support the growth and maintenance of these intense SBC updrafts.

Figures 3a–c show the hourly and vertically averaged θ_E between $z = 200$ and 850 m and hourly averaged vertical velocity at $z = 1.5$ km for hours 19, 20, and 22. During hours 19 and 20, the low-level θ_E has a clear asymmetric structure, with high-θ_E air of the inner core (>360 K) spiraling inward toward the DL quadrant, resulting in a "comma" shape (Figs. 3a,b). Frequently documented in previous studies (Riemer and Montgomery 2011; Riemer et al. 2013; Riemer 2016), this asymmetric high-θ_E region is often referred to as the "moisture envelope" and is a direct result of the wavenumber-1 forcing of the deep-layer wind shear (Riemer and Montgomery 2011). Meanwhile, the hourly averaged updrafts in the boundary layer ($z = 200$–800 m) show a spiral band that coincides with a strong horizontal θ_E gradient at the outer boundary of the moist envelope. One of these updraft zones is located in the DR quadrant, with a spiral pattern that separates the high-θ_E inner-core air from the low-θ_E environment. This DR updraft zone emerged at hour 15 and persisted in a quasi-stationary manner. Another branch of organized updrafts develops and strengthens in the downwind portion of the SBC in the left-of-shear (LS) quadrant during hour 19 (Fig. 3a). This updraft branch appeared as the low-θ_E air to the north advanced southward and strengthened, resulting in a sharper horizontal θ_E gradient here. At hour 20 (Fig. 3b), the LS boundary layer updraft band shifts slightly downwind and becomes more organized and intense, apparently separating from the spiral band in the upwind DR quadrant. Instantaneous model output indicates that these slowly evolving updraft bands are regions supportive of persistent convective activity, where numerous individual convective cells intensify and subsequently propagate downwind during the hour-long period.

Figures 3d–i show the radial–height cross section of θ_E, its vertical gradient, and the secondary circulation, azimuthally averaged over the sectors indicated in Figs. 3a–c. During hours 19 and 20 (Figs. 3d,e), rising motion near 20–40-km radii advects high-θ_E boundary layer air upward, resulting in a column of locally increased θ_E. Throughout this column, the vertical gradient of θ_E remains negative (Figs. 3g,h). Since both the updraft region and the entire layer below 1 km are close to saturation (relative humidity RH $\geq$ 96%; cf. Figs. 3j,k), this indicates that moist absolutely instability is present in the updraft core region. Since θ_E is largely conserved in regions of diabatic heating from condensation, saturated air parcels rising along a negative vertical θ_E gradient gain positive buoyancy due to diabatic heating. This indicates that the continuous diabatic heating release is sustained by the release of moist absolute instability. These results are consistent with Li and Wang (2012), who emphasized the importance of convective available potential energy (CAPE) in driving the updrafts in the rainband region. We also note that after the secondary eyewall has formed at hour 22 (Fig. 3f), the θ_E structure following the updraft zone has notably changed—θ_E contours are more

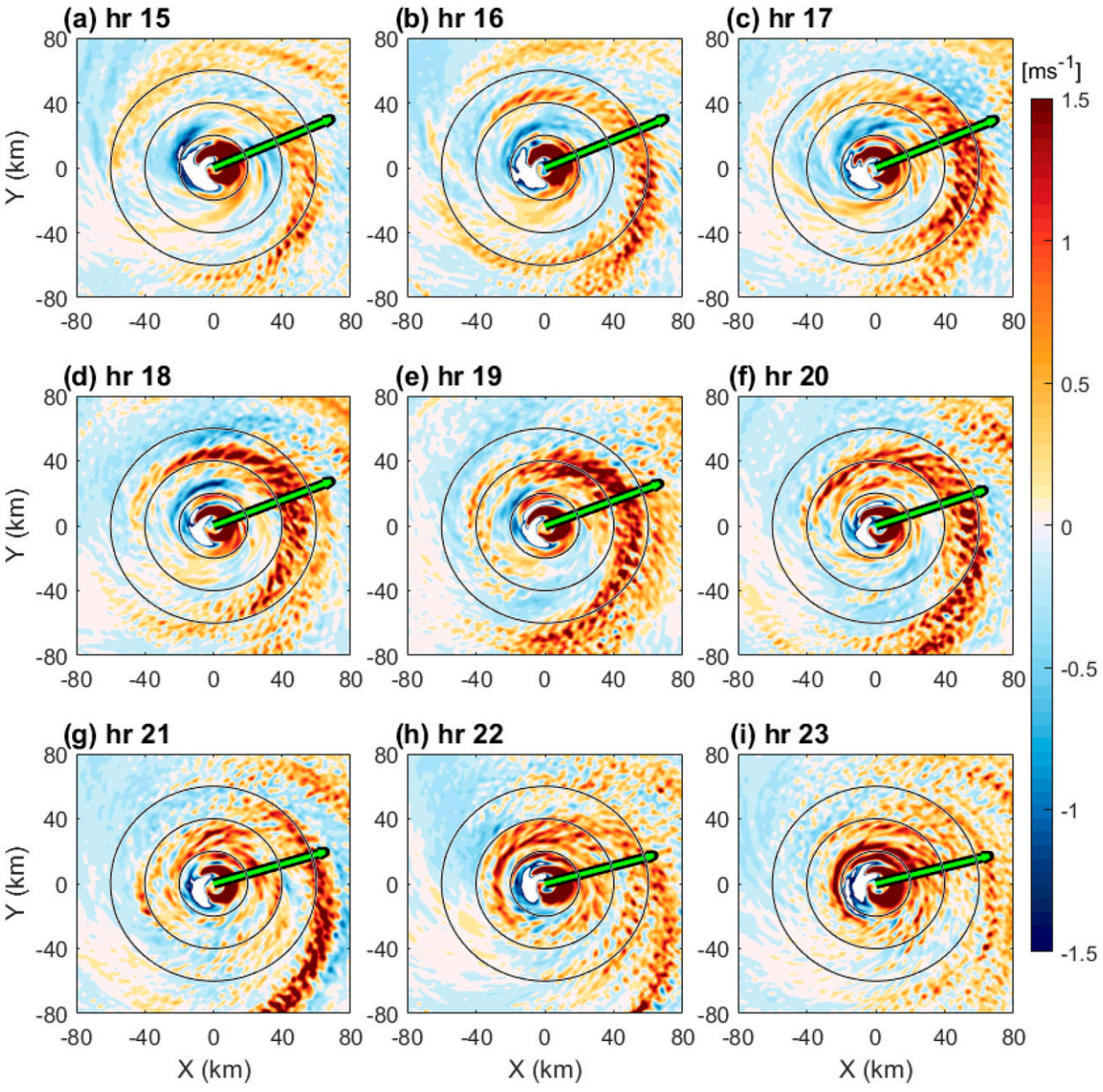

FIG. 2. Plan views of vertical velocity at $z = 4$ km from simulation hours 15 to 23. Green arrows indicate the 850–200-hPa environmental wind shear vector. Black circles indicate 20-, 40-, and 60-km radii. All fields are temporally averaged over the 1-h period starting at the hour mark using 5-min output.

vertically erect, with a weaker vertical gradient. This change indicates that after the establishment of the outer eyewall, the outer eyewall updrafts may not be solely relying on the release of moist absolute instability, but more on the moist symmetric instability (Fig. 3i).

b. A moist instability budget at hours 19 and 20

Given the close association between the enhanced outer updrafts and the release of moist instability, in this section we examine the budget of the moist instability parameter $(\partial\theta_E/\partial z)$ to understand how the persistent updrafts in hours 19 and 20 are sustained in the SBC.[1] Taking the vertical derivative of Eq. (2), the storm-relative budget equation for $\partial\theta_E/\partial z$ is

[1] A more appropriate instability parameter is $(\partial\theta_E/\partial z)_M$, i.e., the vertical change of θ_E along angular momentum surface M. However, a correct $(\partial\theta_E/\partial z)_M$ budget would need to account for M surface changes, making it less ideal for budgeting diagnosis. During hours 19 and 20, $\partial\theta_E/\partial z$ is the dominant part of the $(\partial\theta_E/\partial z)_M$. Therefore, the $\partial\theta_E/\partial z$ budget still provides important insight to the instability evolution during these 2 h.

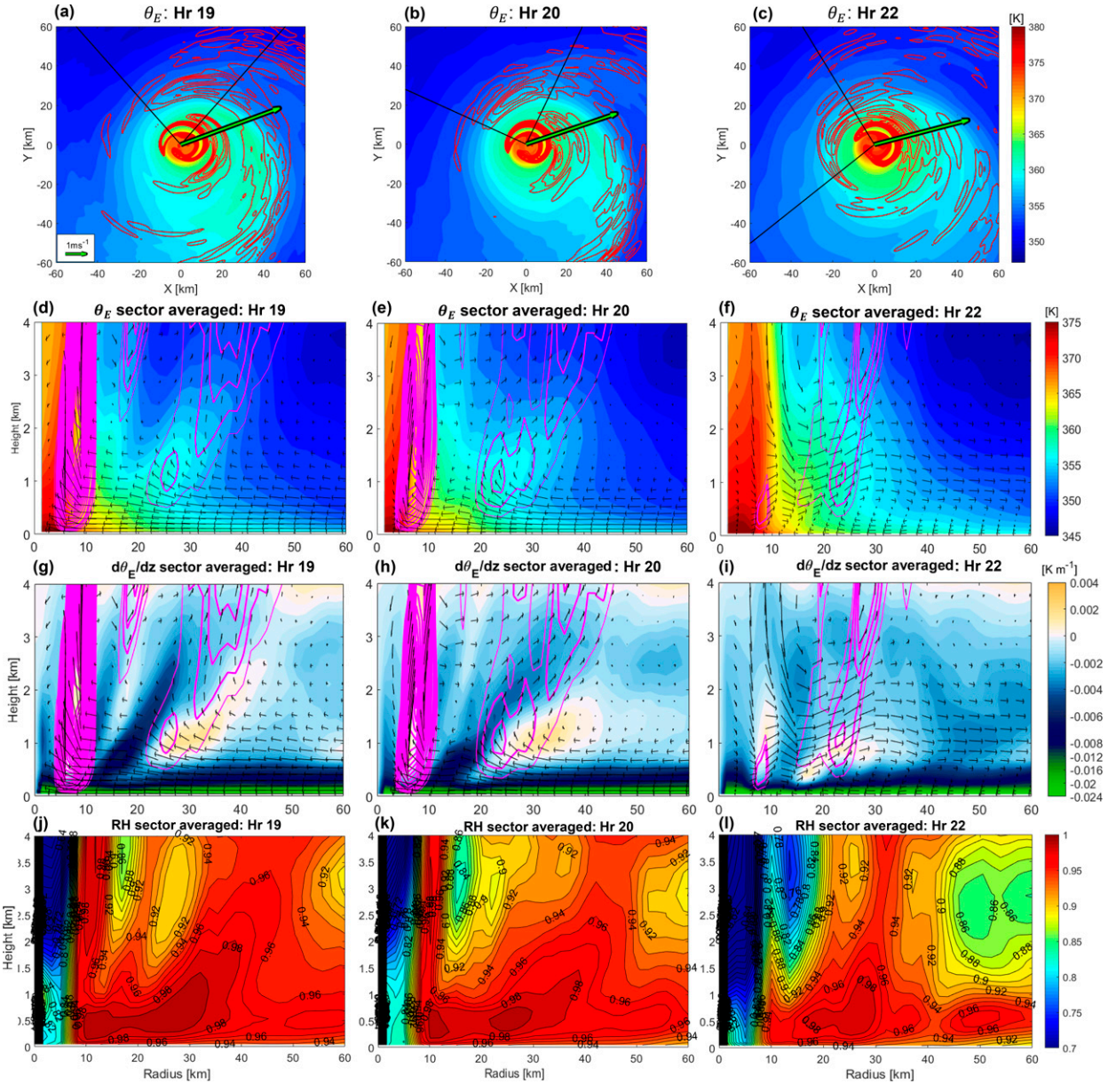

FIG. 3. (a)–(c) Plan views of hourly averaged θ_E (shading) for (a) hour 19, (b) hour 20, and (c) hour 22, vertically averaged over z = 200–850 m. Positive vertical velocity at z = 1.5 km is contoured in red at every 0.4 m s^{-1}. Green arrows indicate the 850–200-hPa environmental wind shear vector. Sectors enclosed by black lines are regions of focus in the subsequent panels. (d)–(f) Cross sections of variables averaged over the sectors and hours shown in (a)–(c). Shown are θ_E (shading), positive vertical velocity (magenta contours every 0.2 m s^{-1} from 0.4 to 3 m s^{-1}), and secondary circulation (radial and vertical velocity) vectors. (g)–(i) As in (d)–(f), but for $\partial\theta_E/\partial z$ (shading) and positive vertical velocity (contours). (j)–(l) As in (d)–(f), but for relative humidity (%).

$$\frac{\partial}{\partial t}\left(\frac{\partial \theta_E}{\partial z}\right) = -\frac{\partial}{\partial z}(\mathbf{v}\cdot\nabla_h\theta_E) - \frac{\partial}{\partial z}\left(w\,\frac{\partial \theta_E}{\partial z}\right) + \frac{\partial F_{\theta_E}}{\partial z}, \qquad (4)$$

where the second and third terms represent the differential horizontal advection (DHA) and differential vertical advection (DVA) effects on the stability parameter. Figure 4 shows the budget terms of Eq. (4), temporally averaged over an hour using 1-min model output and azimuthally averaged over the selected sectors at hours 19 and 20. As shown in Figs. 4a and 4b, the local time derivative of $\partial\theta_E/\partial z$ has relatively small magnitudes compared to the other terms within the updraft region, indicating that the DVA, DHA, and external forcing terms remain quasi balanced to maintain a slowly varying moist instability ($\partial\theta_E/\partial z$) during these 1-h periods. Below 1-km altitude, the dominant balance is between DHA (Figs. 4c,d) and external

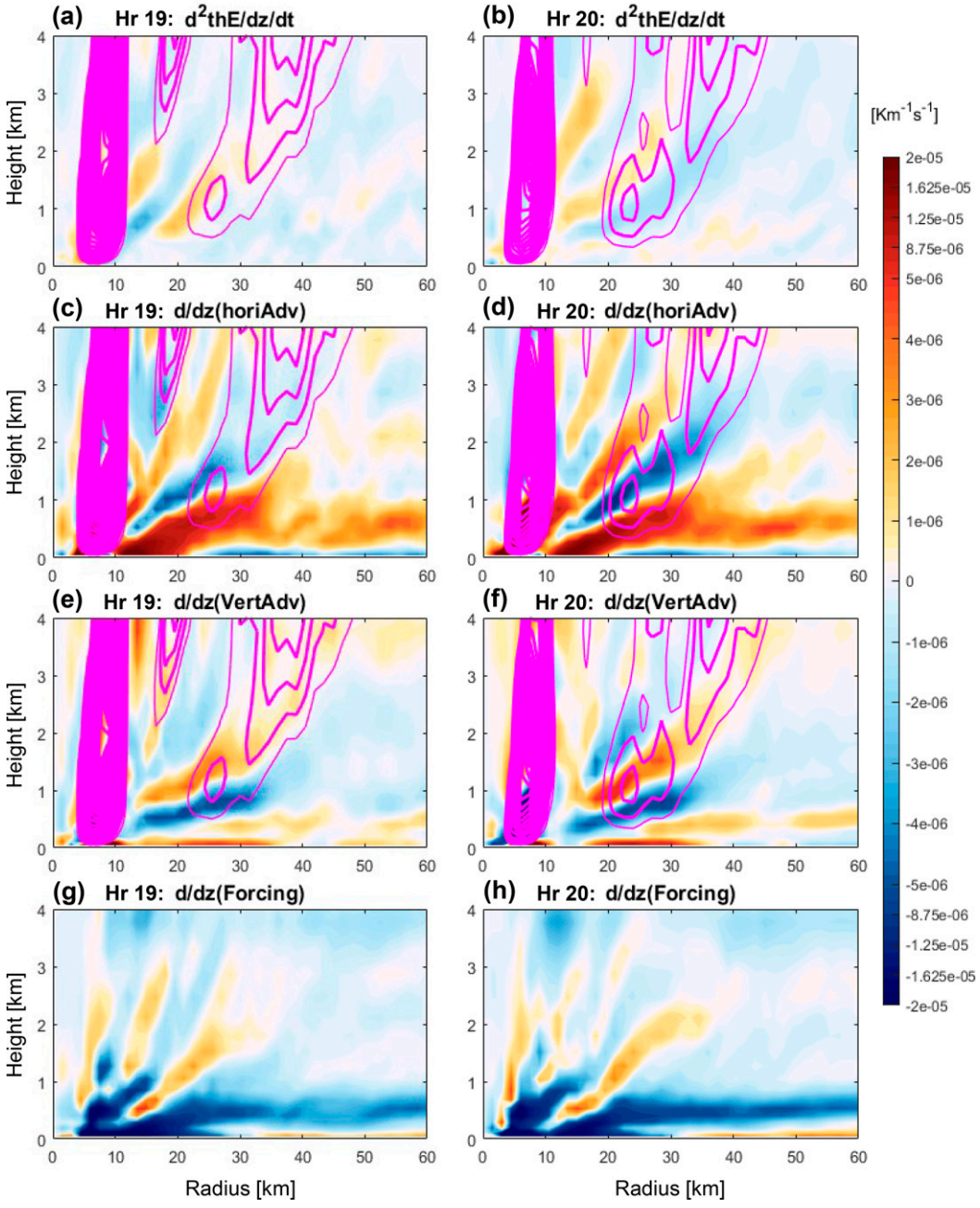

FIG. 4. Hourly averaged cross sections of the terms of the budget equation for $\partial\theta_E/\partial z$ for sectors in Fig. 3 at (left) hour 19 and (right) hour 20. Budget terms are (a),(b) local tendency of $\partial\theta_E/\partial z$, (c),(d) vertical gradient of horizontal advection, (e),(f) vertical gradient of vertical advection, and (g),(h) vertical gradient of θ_E forcing. The corresponding average positive vertical velocity is contoured in magenta every 0.2 m s^{-1} from 0.4 to 3 m s^{-1}, with thickened contours for 0.6 m s^{-1} and greater.

forcing from boundary layer fluxes (Figs. 4g,h). Boundary layer enthalpy fluxes from the warm ocean surface tend to destabilize (i.e., negative tendency values) the boundary layer. This enthalpy is immediately carried away by horizontal advection, thus stabilizing (i.e., positive tendency) the boundary layer air.[2]

[2] We note that the balance between DHA and external forcing is reversed at $z < 300$ m because the subgrid-scale moisture flux convergence attains a maximum near 300 m for $r > 30$ km. Since our main emphasis is on the convective updraft region with strong diabatic heating release, our discussion here focuses on the overall balance throughout the boundary layer.

Focusing on the intense updraft above $z = 1$ km (thick magenta contours), the dominant balance is between DHA and DVA. In Figs. 4e and 4f, DVA is largely positive at the updraft core, indicating that the intense updrafts stabilize the local atmosphere by continuously bringing high-θ_E air from low levels upward. Given that the $\partial\theta_E/\partial z$ at the updraft core region is about -2×10^{-3} K m^{-1} (Figs. 3g–i) and the corresponding DVA is 2×10^{-6} K m^{-1} s^{-1}, such a DVA stabilization rate due to the updraft could deplete the local moist instability in roughly 1000 s (~15 min) if the mechanism to replenish the instability is absent. However, the intense updraft region in the LS sector not only lasts for more than 2 h, the local instability during this period also remains slowly varying during hours 19 and 20 (Figs. 3g,h). This indicates that a continuous supply of moist instability must exist in the vicinity to maintain the longevity and strength of the updrafts. The budget analysis shows that above $z = 1$ km, DHA is the only source of destabilization that can counter the stabilization inherent to the vertical θ_E advection by the intense updrafts. In other words, if this destabilizing mechanism does not exist (i.e., small DHA), the positive DVA will simply result in positive $(\partial/\partial t)(\partial\theta_E/\partial z)$, i.e., a weakening of local moist instability and thus the convective activity. Therefore, the quasi-balanced relationship in the $\partial\theta_E/\partial z$ budget suggests that the destabilization from DHA is essential for sustaining the continuous diabatic heating in the long-lasting convective updraft zone.

To examine the DHA structure more closely, Figs. 5a–c show the cross sections of DHA at hour 20 decomposed into its azimuthal and radial advection components. The result for hour 19 is similar and is therefore not shown. Focusing on the updraft core between $z = 0.8$ and 1.5 km, the destabilization of the DHA term is largely the result of differential azimuthal advection. Differential radial advection has a more varied contribution at this altitude since below $z = 1$ km, stabilization occurs from inward advection of the surface high-θ_E air. Above 2 km, differential radial advection also provides an important destabilization source as the radial outflow of convection transports high-θ_E inner-core air outward.

Figures 5d–f show the plan views of vertically integrated (between $z = 1$ and 3.3 km) DHA and the two components. Note that the vertical integration of DHA equals to the difference of horizontal advection between the layer top and bottom, that is,

$$\int_{z_{\text{bottom}}}^{z_{\text{top}}} \frac{\partial}{\partial z}(-\mathbf{v}\cdot\nabla\theta_E)\,dz = (-\mathbf{v}\cdot\nabla\theta_E)\big|_{z_{\text{top}}} - (-\mathbf{v}\cdot\nabla\theta_E)\big|_{z_{\text{bottom}}}. \tag{5}$$

From Fig. 5d, the layer-mean DHA indeed provides strong destabilization throughout the entire rainband region, which means that DHA results in differential warming of θ_E that is stronger at the layer bottom ($z = 1$ km) than the layer top ($z = 3.3$ km). This destabilization is crucial since it replenishes the moist instability in the rainband region that would otherwise be depleted by the stabilization effect of the intense rainband updrafts, thus maintaining the strong convective updraft zone in a quasi-stationary manner over a long duration.

The two horizontal components (Figs. 5e,f) further show that the destabilization effect mainly comes from azimuthal advection, which is partially offset by the radial component. Since the θ_E contours take a spiral pattern (Fig. 3b), this partial cancellation indicates that the horizontal wind field crosses the θ_E contours from warm to cold cyclonically.

To consolidate the relationship between DHA and w, we focus on updrafts at the rainband region ($r > 20$ km) that are greater than 0.4 m s^{-1} and examine the statistics between w and DHA (Fig. 5g), its azimuthal component (Fig. 5h), and its radial component (Fig. 5i). As seen in Fig. 5g, not only is the centroid (or maximum) of the distribution located at the negative half plane of DHA, but vertical velocity also displays a clear negative correlation with DHA. These implies that more intense updrafts tend to occur at regions with more negative DHA (i.e., a stronger destabilization effect). When separated into the azimuthal and radial advection components, we see that the major contributor of the destabilization effect comes from the azimuthal advection, consistent with Figs. 5b and 5e.

c. *Features responsible for the destabilization by differential horizontal θ_E advection*

Given the importance of the destabilization by DHA, we next examine the processes that lead to this destabilization. Figure 6a shows the plan view of asymmetric θ_E at hour 20 averaged between $z = 200$ and 850 m and the sectors (located DR and LS) analyzed in Figs. 6b–d. Figure 6b shows the cross section of θ_E, vertical velocity, and vectors representing azimuthal advection of θ_E [i.e., $-(v/r)(\partial\theta_E/\partial\lambda)(\hat{\lambda})$] over the left-of-shear updraft region between $r = 20$ and 30 km. Below $z = 1.25$ km, a strong azimuthal gradient in θ_E is located near 350°, with warm θ_E air located azimuthally upwind. Collocated with this strong θ_E gradient is the updraft maximum. As expected, azimuthal advection of θ_E is strong where the azimuthal θ_E gradient is steep. More importantly, this warm advection of θ_E is decreasing with height between 0.5 and 2 km, resulting in differential warming of θ_E that effectively replenishes the local moist instability that would have been otherwise depleted by the strong updrafts. Shown in Fig. 6a, the low-θ_E air on the downwind side of the LS updraft is associated with a surface cold pool that intrudes inward and sets up the azimuthal θ_E gradient. The core of this cold pool can also be seen in Fig. 6b near 305°. Figure 6d shows the radius–height cross section averaged over the LS sector. Seen here, the negative θ_E anomaly of the surface cold pool is connected to downdrafts that originate from the midtroposphere near 4–5-km altitude. These downdrafts are driven by stratiform diabatic cooling that cover beyond $r = 120$ km. This shows that the tight horizontal θ_E gradient seen in Fig. 3b is caused by the interaction between the surface cold pool and the inner moist envelope.

Figure 6c shows the azimuth–height plot over the rainband updraft region in the DR sector. The updraft here, similar to that in Fig. 6b, is located in a region of vertically decreasing azimuthal advection of θ_E. However, one key difference is that the azimuthal θ_E gradient does not involve a mesoscale

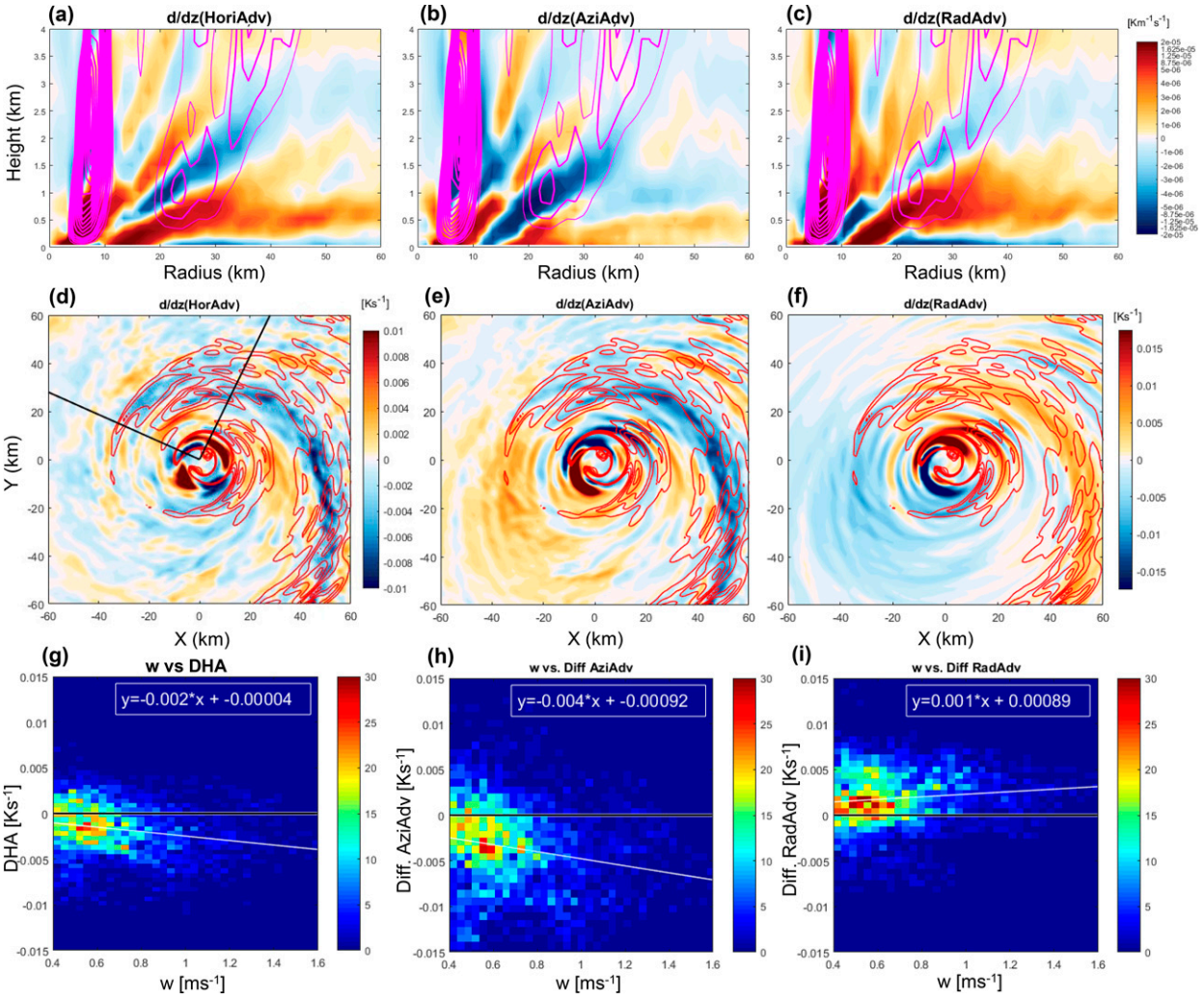

FIG. 5. (a)–(c) As in Fig. 4, but for the vertical gradient of (a) horizontal advection, (b) azimuthal advection, and (c) radial advection for hour 20 in the sector shown in (d). (d)–(f) Plan view of the quantities in (a)–(c), vertically integrated between $z = 1$ and 3.3 km. Positive vertical velocity is contoured in red every 0.2 m s^{-1}. (g) Histogram of vertically integrated w vs differential horizontal advection (DHA) between $z = 1$ and 3.3 km, as shown in (d). Only data points with $r > 20$ km and $w > 0.4$ m s^{-1} are collected. Best linear fit is plotted in the straight white line with the equation shown. Zero value is shown as the black solid line. (h),(i) As in (g), but for w vs differential azimuthal advection, and w vs differential radial advection, respectively.

cooling-induced surface cold pool. As shown in Fig. 6e, the weak negative anomaly of θ_E in the DR does not reach the surface and is not collocated with a downdraft and diabatic cooling. Rather, this azimuthal gradient represents the boundary between the TC moist envelope of high-θ_E air and the colder environmental air. So, while the destabilization mechanisms are similar in both the DR and LS updraft regions, the physical origins that lead to the destabilization are different.

d. *Updraft initiation*

Given the close association between the LS intense updraft zone and the surface cold pool, it is important to further examine the role of the surface cold pool on the initiation of the convective updraft. As was shown in section 4a, since the updraft zone in the LS is embedded in a conditionally unstable atmosphere ($\partial\theta_E/\partial z < 0$), once the lifted condensation level is reached, the upward acceleration of the air parcel soon becomes buoyancy driven (due to diabatic heating release) and relies on the release of moist instability. Therefore, this analysis focuses on the lifting process before any diabatic heating release occurs. Trajectory calculations are performed offline using the Lagrangian Analysis Tool (Lagranto; Wernli and Davies 1997; Sprenger and Wernli 2015) with WRF Model output at 1-min interval. The trajectories are initialized every 5 min during a 30-min time window from $t = 20$ h 15 min to $t = 20$ h 45 min in the LS updraft zone for grid points with $w > 0.2$ m s^{-1} at $z = 90$, 120, 150, and 180 m. At each initial point, 10-min forward and 15-min backward trajectories are calculated, yielding a 25-min trajectory for each point ($t = -15$ to $+10$ min). To focus on the

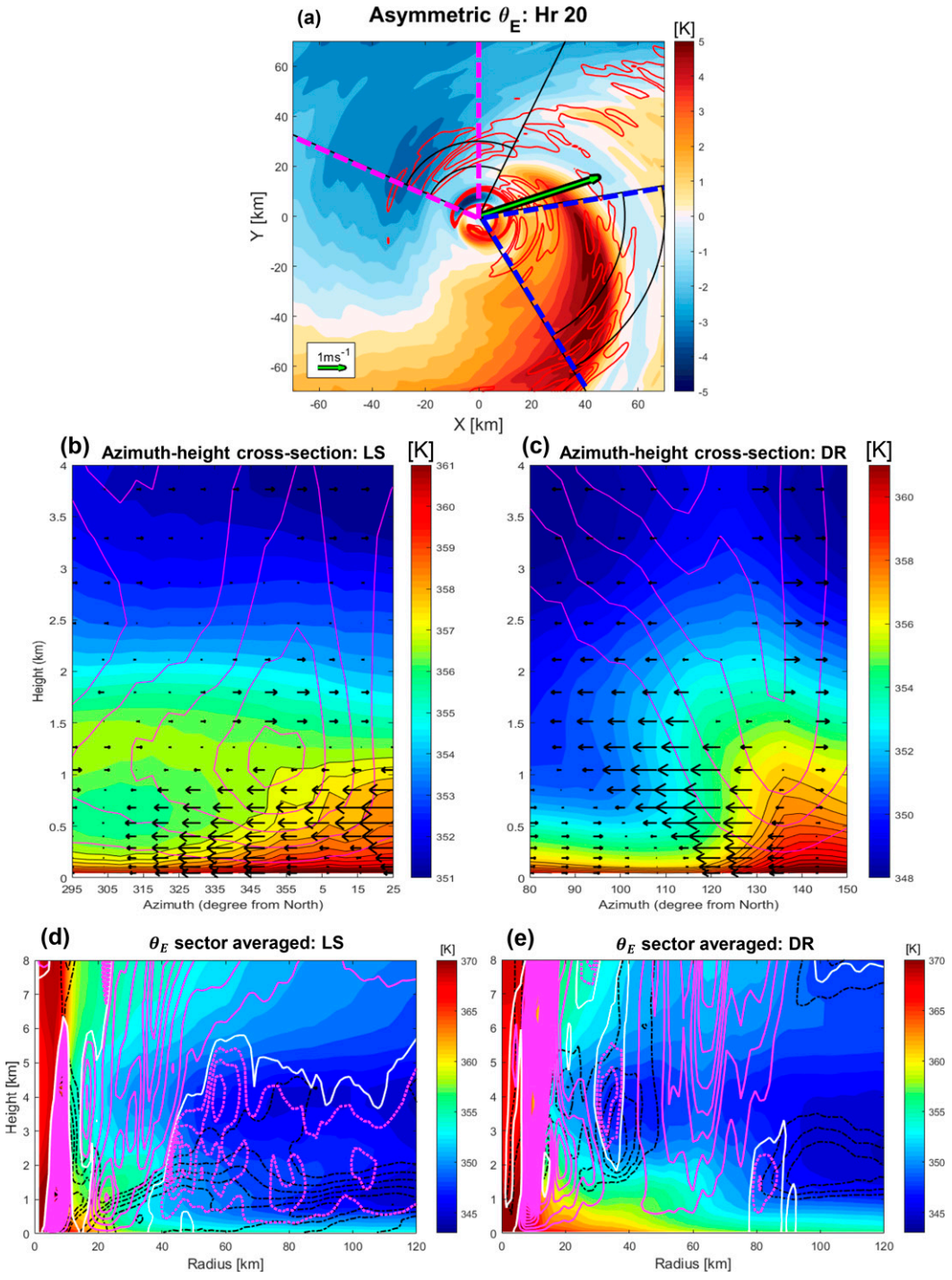

FIG. 6. (a) Plan view of hourly averaged asymmetric θ_E for hour 20, vertically averaged between z = 200 and 850 m. Positive vertical velocity at z = 1.5 km is contoured in red every 0.4 m s^{-1}. Black lines and arcs indicate azimuthal and radial ranges of averaging used in (b) and (c). The sector enclosed by the magenta and blue dashed lines shows the range of azimuthal averaging used in Fig. 7. (b) Azimuth–height cross section of hourly averaged θ_E for hour 20, radially averaged between r = 20 and 30 km over the sector highlighted left-of-shear (LS) sector in (a). Positive vertical velocity is contoured in magenta every 0.25 m s^{-1}. Vectors indicate azimuthal advection of θ_E, with warm advection pointing to the decreasing azimuth direction. (c) As in (b), but for the downshear-right (DR) sector highlighted in (a), radially averaged between r = 55 and 70 km. (d) Radial–height cross section over the LS sector of hour 20 for θ_E (shading), negative θ_E anomaly (black dashed contours every 0.5 K), updraft (solid magenta every 0.12 m s^{-1}), and downdraft (dashed magenta every 0.06 m s^{-1}). Zero vertical velocity is contoured in white. (e) As in (d), but for the DR sector.

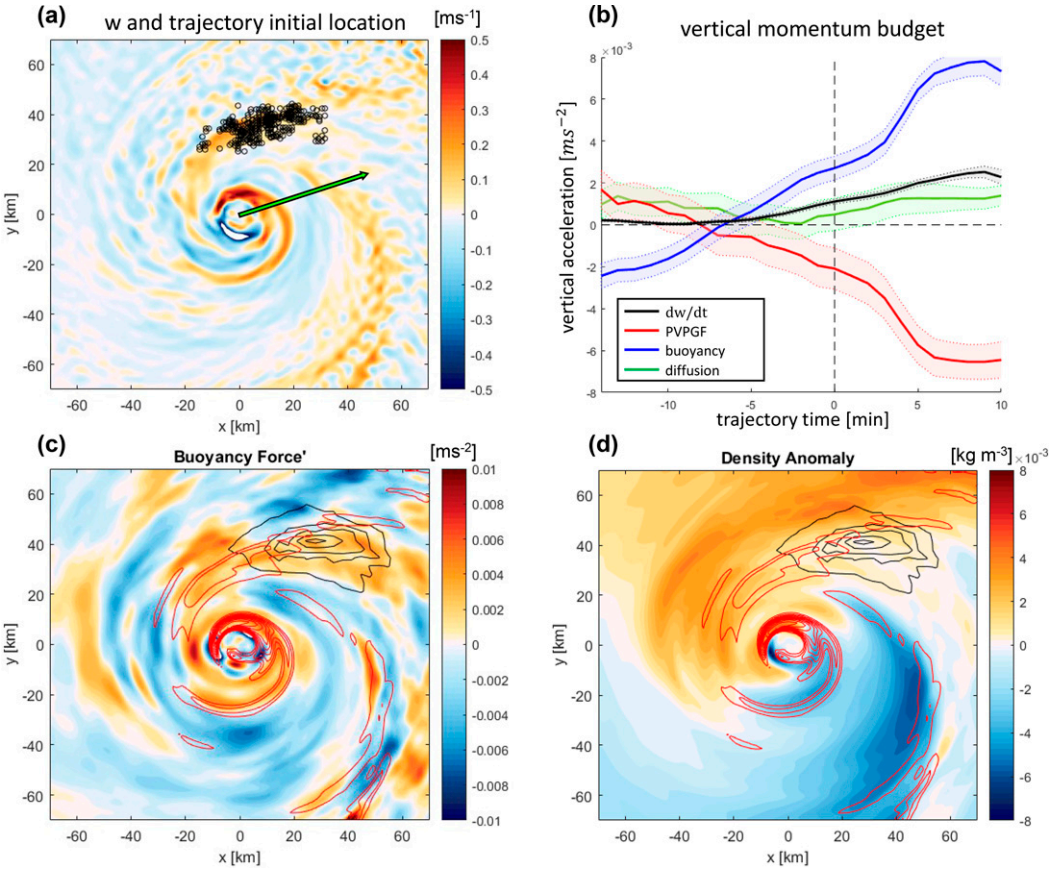

FIG. 7. (a) Plan view of vertical velocity at $z = 100$ m, temporally averaged from $t = 20$ h 15 min to 20 h 45 min. The black dots show the storm-relative initial locations of the trajectory calculations that satisfy the minimum updraft and diabatic heating criteria (see text for details). The total number of the trajectories is 779. The green arrow indicates the direction of the deep-layer wind shear. (b) Time series of the Lagrangian vertical momentum budget terms for the trajectories, composited with respect to the trajectory initial time (at $t = 0$ min). The shaded region shows $\pm 2\sigma_{\text{mean}}$ of each term, where σ_{mean} is the standard deviation for the composite mean. (c) Plan view of the buoyancy force, vertically averaged below $z = 400$ m. Black contours show the normalized backward trajectory histogram. The histogram is normalized by its maximum value and is contoured every 0.1 from 0.05 to 1. Positive vertical velocity, vertical averaged below $z = 400$ m, is contoured 0.15 m s^{-1} in red. (d) As in (b), but for asymmetric density anomaly vertically averaged below $z = 400$ m.

intense updraft, only the trajectories satisfying the following criteria will be composited and analyzed. First, we require the mean updraft over the 25-min trajectory to be at least 0.4 m s^{-1}. Second, to isolate the updraft lifting mechanism solely due to buoyancy induced by diabatic heating release, we require the trajectory to have no positive diabatic heating release from $t = -15$ to -1 min. Among these trajectories, it is found that over 85% of the trajectories (779 trajectories) experience lifting during the first 15 min of the trajectory [$z(t = -15 \text{ min}) > z(t = -1 \text{ min})$], despite diabatic forcing being nonpositive. Figure 7a shows the plan view of the storm-relative initial locations of the trajectories, together with the vertical velocity at $z = 100$ m averaged from $t = 20$ h 15 min to 20 h 45 min. To examine the lifting mechanism, the following Lagrangian vertical momentum equation budget is computed along the trajectories

$$\frac{dw}{dt} = \left(-\frac{1}{\rho_0}\frac{\partial p^*}{\partial z} + F_{\text{curv,coriolis}} \right) + \frac{\rho^*}{\rho_0} g + F_{\text{diff}}, \qquad (6)$$

where the asterisk denotes deviation from hourly averaged field; the terms on the right-hand side are the perturbation vertical pressure gradient force (PVPGF), curvature and nontraditional Coriolis forces, buoyancy force (B), and diffusion. It is found that part of the PVPGF is strongly balancing the curvature and nontraditional Coriolis forces (analogous to geostrophic balance). Therefore, these two terms are grouped together to form the effective PVPGF (e.g., $-(1/\rho_0)(\partial p^*/\partial z) + F_{\text{curv,coriolis}}$). Note that both the PVPGF and buoyancy force are defined as deviation from some hydrostatic reference state. Smith et al. (2005) illustrated the ambiguity in defining this hydrostatic reference state in a gradient-wind environment that incorporates asymmetric storm features. Given the asymmetric structure

of the mass fields in the outer-core rainband region, we used the hourly averaged density and pressure fields from $t = 20.0$ to 21.0 h to define the hydrostatic reference state. This yields a three-dimensionally varying hydrostatic reference state that best captures both the system buoyancy of the axisymmetric balanced vortex (Smith et al. 2005) and the outer-core asymmetric structure of the balanced mass fields (e.g., the quasi-stationary cold pool in the LS quadrant).

Figure 7b shows the 5-min running averaged time series of the vertical momentum budget, composited with respect to $t = 0$ min of each trajectory. Focusing on the time from $t = -15$ to -1 min, the vertical velocity tendency is increasingly positive (upward acceleration) during $t = -5$ to -1 min. Since diabatic forcing (from microphysics) is nonpositive, the lifting of these air parcels is not driven by diabatic heating release. However, these air parcels indeed acquire positive buoyancy during $t = -5$ to -1 min, which outweighs the negative PVPGF. Since the vertical diffusion is small compared to the vertical acceleration, this means that the positive buoyancy of these air parcels is instrumental to the lifting process. And as expected, after $t = 0$ min, the positive buoyancy and vertical acceleration are further enhanced by strong diabatic heating release.

Figures 7c and 7d show the plan views of buoyancy and density anomaly vertically averaged below $z = 400$ m, along with frequency contours of the trajectories from $t = -15$ to -1 min. From Fig. 7c, the trajectories during the vertical lifting period are collocated exactly with a region of positive buoyancy, which is connected with the LS updraft zone and forms a continuous band. Looking at Fig. 7d, this positive band of buoyancy is located on the inward and immediately upwind side of a widespread positive density anomaly that covers the LS quadrant, which is also associated with a negative anomaly of θ_E, i.e., the stationary surface cold pool (as shown in Fig. 6a). This band of positively buoyant air (with respect to the hourly balanced mass fields) on the upwind edge of the surface cold pool indicates that as the TC inner-core air parcels travel cyclonically and encounter the stationary cold pool in the LS quadrant, they acquire positive buoyancy due to the density contrast and are lifted upward along the inner edge of the surface cold pool.

The dynamics of the lifting process and its placement relative to the surface cold pool agree well with the buoyancy advection mechanism described in Yu and Didlake (2019). Using idealized simulations of a dry, hurricane-like vortex, Yu and Didlake (2019) examined the vortex response to a prescribed stratiform diabatic forcing that mimicked a TC spiral rainband. They used a generalized omega equation to diagnose the vertical velocity responses in the vortex. They showed that a long-lasting spiral updraft band emerges on the upwind side of the cooling-driven cold pool as a result of buoyancy advection at that region. This buoyancy advection relies on the horizontal density gradient set up by the stationary cold pool, a key ingredient that is well captured in Figs. 6a, 6d, and 7d. They also demonstrated that the updraft driven by this mechanism is strong enough to lift the air parcel to its lifted condensation level and potentially trigger a buoyant updraft. This claim is supported by Fig. 7c, where we see that the buoyancy force at the lifting region and updraft region forms a continuous spiral band, indicating a clear connection between these two features. Given the results of our trajectory analysis and the similarity in the updraft placement with respect to the surface cold pool, we believe that the buoyancy advection mechanism described in Yu and Didlake (2019) plays an important role in the lifting process identified in the current simulation.

5. The PV evolution and budget

The previous sections demonstrated how stratiform diabatic processes in the downwind rainband sector help to initiate convective updrafts and create a thermodynamic environment conducive for sustaining organized, persistent convection. However, the exact connection between these updrafts and the formation of the secondary eyewall remains unclear. Our Hovmöller (Fig. 1a) and plan view (Fig. 2) analyses strongly suggests that the outer eyewall is axisymmetrized from the asymmetric updrafts at the left-of-shear quadrants. Following this idea, several important questions regarding the roles of these asymmetric updrafts in the axisymmetrization process still need to be answered. Specifically, does the axisymmetrization process occur in the form of the cyclonic downwind propagation of these asymmetric updrafts? And why does axisymmetrization occur only after the MDI reaches the boundary layer in the LS quadrant and develops the surface cold pool, but not earlier? To examine these questions and to further understand the role of these updrafts in the axisymmetrization process, we now examine the PV evolution and budget. We choose to examine the PV in this analysis since PV is a physical quantity that incorporates the evolution of both the dynamical and thermodynamic properties of the flow. Numerous studies (e.g., Judt and Chen 2010; Wang et al. 2019) show that secondary eyewall formation is marked by the gradual formation of a concentric ring of PV maxima outside the primary eyewall, and therefore is particularly suitable for this analysis.

a. PV evolution during the SEF period

Figure 8 shows the hourly averaged azimuthal mean PV structure during hour 15 and its subsequent evolution (changes relative to hour 15) from hours 16 to 23, along with positive vertical velocities. At hour 15 during the early phase of the SEF period, high PV values (>50 PVU; 1 PVU = 10^{-6} K kg^{-1} m^2 s^{-1}) are concentrated at the eye, and decay to below 3 PVU outside 25-km radius. During hours 16–18, when the SBC is intensifying, the symmetric PV changes outside 20-km radius are generally small. At hour 19 when the convective updrafts emerge in the LS quadrant, the symmetric PV shows a clear increase between 30- and 40-km radii and between 4- and 10-km altitude. During hour 20, this increase of the symmetric PV becomes stronger and extends into the lower levels. This PV increase at 20–40-km radius continues during hour 21. At hour 22, the secondary eyewall is established with a strong outer updraft maximized at 20-km radius.

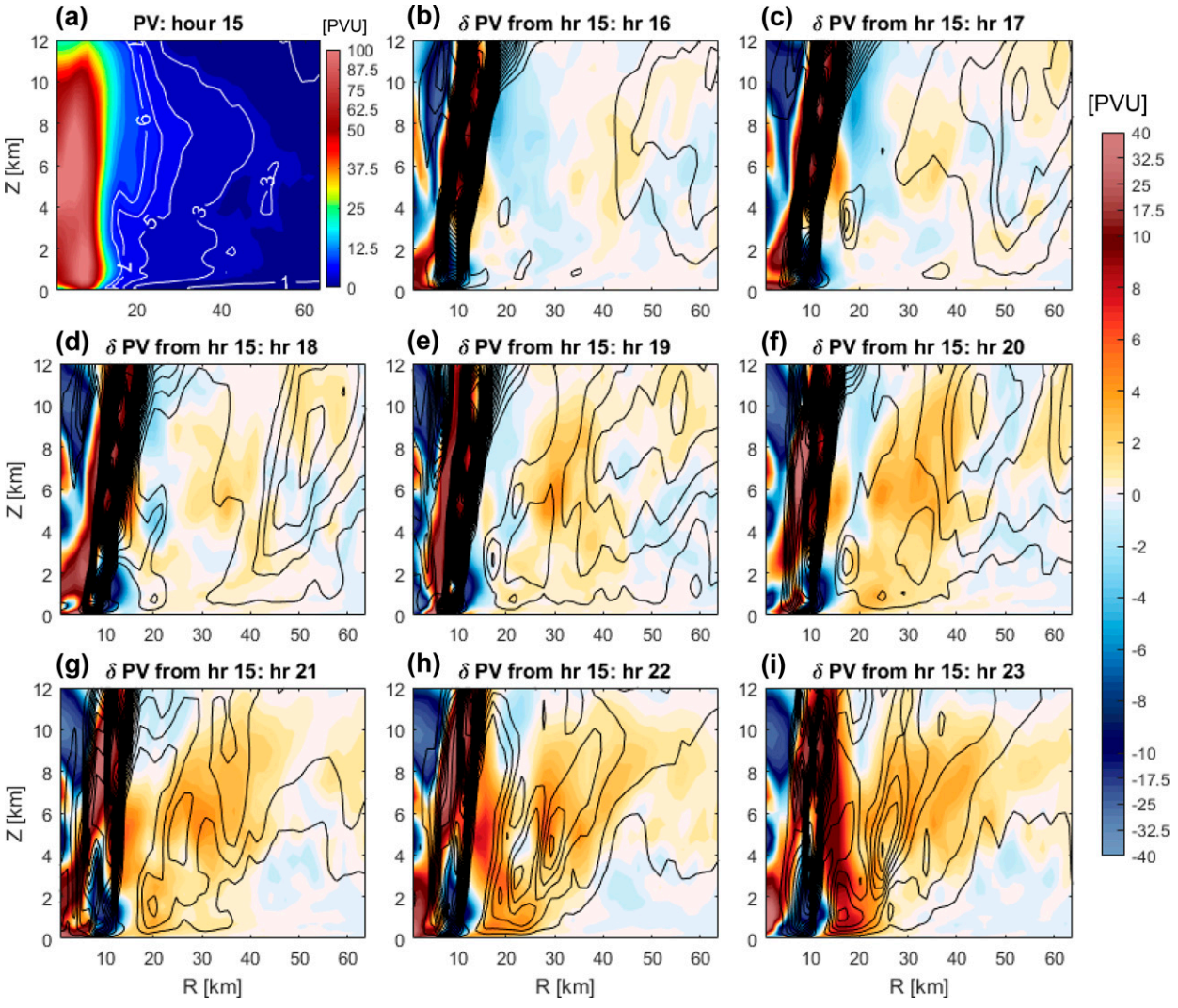

FIG. 8. (a) Cross section of hourly averaged azimuthal mean PV for hour 15. PV less than 9 PVU is contoured in white every 2 PVU. (b)–(i) Cross section of the changes in hourly averaged azimuthal mean PV relative to hour 15. Positive vertical velocity is contoured in black at every 0.15 m s^{-1}.

To illustrate the temporal evolution of PV associated with the emerging outer eyewall, Fig. 9a shows a radius–time plot of the axisymmetric PV changes at $z = 2$ km relative to the hourly average at hour 15. Consistent with Fig. 8, the axisymmetric PV at 20–40-km radius notably increases around hour 20. The increase in the axisymmetric PV in the outer eyewall region can be further illustrated using the axisymmetricity parameter (AP; Miyamoto and Takemi 2013), defined as

$$\mathrm{AP} = \frac{|\overline{P}|^2}{|\overline{P}|^2 + |P'|^2}, \tag{7}$$

where $|\overline{P}|^2 = \sum_i \overline{P}_i^2$ and $|P'|^2 = \sum_i P_i'^2$ are the norm square of the symmetric and asymmetric PV with i being the grid points within a specific radial range. The temporal evolution of AP can be properly analyzed when the selected radial range best captures the inward contracting PV that eventually axisymmetrizes into an outer eyewall. To do this, we first identify regions at radius $r > 15$ km where the increase in total PV magnitude $\left(\text{i.e., } \sqrt{|\overline{P}|^2 + |P'|^2}\right)$ relative to hour 15 is greater than 3 PVU. From these locations, the radius of maximum AP is determined at each time. For times earlier than hour 18, the 3 PVU threshold criterion is disregarded and only the outer PV maximum radius is identified. The result of this procedure is an inward contracting radial location that captures the PV signal associated with the forming outer eyewall (Fig. 9a).

Figure 9b shows the actual and hourly averaged temporal evolutions of AP along our identified inward contracting line. During hours 16–18, the AP has small values between 0.2 and 0.3, indicating that the outer-core PV is largely asymmetric. Between t = 19 and 20 h (when the 20–40-km axisymmetric

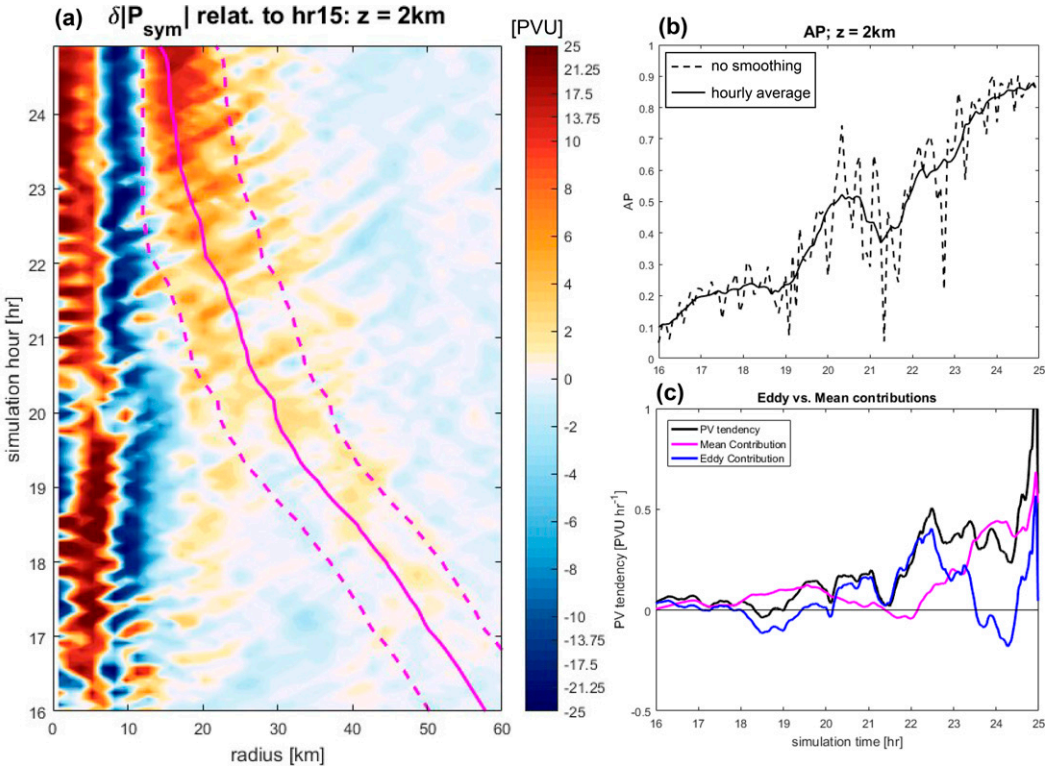

FIG. 9. (a) Hovmöller diagram of the change in azimuthal mean PV relative to hour 15, and the radial location of the axisymmetrizing PV (solid magenta line; see text for detailed description). The dashed magenta lines indicate the range of radial averaging of the PV budget shown in (c). (b) Time series of the axisymmetric parameter (AP) along the axisymmetrizing PV line in (a). (c) Time series of hourly averaged total density-weighted PV (q) tendency, and the contributions from mean and eddy processes, radially averaged over the dashed magenta lines in (a) and vertically averaged over z = 0.5–8 km.

PV strongly increases), the AP abruptly increases from 0.2 to 0.5. While fluctuations exist near t = 21 h, which results in an episodic decrease of AP from 0.5 to 0.4, the AP further increases to 0.6–0.7 during at t = 22–23 h. After t = 23 h, AP values remain steady near 0.8–0.9, indicating the establishment of the secondary eyewall, which is consistent with our defined SEF timing at hour 22. Given that the AP shows a clear increase starting from t = 19 h before the establishment of the secondary eyewall at hour 22, we now define the time period of "axisymmetrization" to be the time window between t = 19.0 and 22.0 h.

To quantify the dynamical processes contributing to the azimuthal mean PV, the PV equation, Eq. (3), is rewritten into the density-weighted flux divergence form and then separated into mean flow and eddy terms:

$$\frac{\partial \overline{q}}{\partial t} = -\frac{1}{r}\frac{\partial r\overline{q}\,\overline{u}}{\partial r} - \frac{\partial \overline{q}\,\overline{w}}{\partial z} - \frac{1}{r}\frac{\partial r\overline{q'u'}}{\partial r} - \frac{\partial \overline{q'w'}}{\partial z} + \overline{F_{q,\mathrm{mean}}} + \overline{F_{q,\mathrm{eddy}}}, \tag{8}$$

where $q = \rho P$ is the density-weighted PV, u is the radial velocity, the overbar denotes azimuthal average, and the prime denotes deviation from the azimuthal mean. The first and second terms on the right-hand side of Eq. (8) are radial and vertical convergence of azimuthal mean (symmetric) PV flux; the third and fourth terms are the radial and vertical convergence of eddy (asymmetric) PV fluxes; and the fifth $\left(\overline{F_{q,\mathrm{mean}}} = \nabla \times \overline{\mathbf{F}} \cdot \nabla\overline{\theta_\rho} + \zeta \cdot \nabla\overline{\dot{\theta}_\rho}\right)$ and sixth terms $\left(\left[\overline{F_{q,\mathrm{eddy}}} = \overline{(\nabla \times \mathbf{F}') \cdot \nabla\theta'_\rho} + \overline{\zeta'} \cdot \nabla\dot{\theta}'_\rho\right]\right)$ are the forcing contributed by the mean and eddy quantities, respectively. These terms are first analyzed within the radially contracting outer PV region enclosed by the dashed lines in Fig. 9a, which is 15-km wide and centered on the inward contracting line (except for later times when the inner bound becomes fixed to avoid the primary eyewall PV). Figure 9c shows the time series of the axisymmetric PV tendency, and the corresponding mean and eddy contributions vertically averaged between z = 0.5 and 8 km. The total axisymmetric PV tendency is small during t = 16–18 h but begins a clear increasing trend during t = 19–22 h. During t = 19–20 h, the mean contribution stays at a steady positive value but starts to decline gradually to near zero during t = 20–22 h. On the other hand, the eddy contribution first starts with negative value during t = 18 h due to the outward slantwise structure of updrafts at the developing SBC near the DL quadrant (Yu et al. 2021). Starting from t = 19 h, the eddy contribution increases to small positive values, surpasses the mean

contribution near hour 20, and continues the steady increase during t = 20–21 h. Despite an episodic drop during t = 21–21.5 h, the eddy contribution continues to increase to large positive values during t = 21.0–22.0 h. Because of the general declining trend of the mean contribution during t = 19–22 h, the increasing trend of eddy contribution closely resembles that of the total axisymmetric tendency during this axisymmetrization period. Despite a negative eddy contribution during t = 18.0–19.5 h, the resemblance between eddy and total PV tendency indicates that the PV generated by eddy processes can project onto the azimuthal mean and shapes the systematic increase of the total axisymmetric PV during this period. As will be shown in section 5c, these eddy processes are due to the enhanced rainband convection in the LS and UL quadrants.

Near t = 22.5 h, the opposite pattern occurs with the eddy contribution decreasing and the mean contribution increasing and surpassing the eddy contribution. This pattern is consistent with our definition of SEF timing at hour 22 based on vertical velocity. After t = 23 h, the mean contribution continues to grow, indicating that the axisymmetric dynamics dominate the evolution afterward.

Returning to Fig. 8, another notable feature is a small updraft occurring between 15- and 20-km radius and between 2- and 4-km altitude during hours 16–20. Nearby is a small region of increased PV at 15-km radius between 4- and 6-km altitude. These features are likely the manifestations of VRWs propagating outward from the primary eyewall, which then halt at a stagnation radius. Several studies have attributed this VRW process to SEF, since at this stagnation radius, the waves deposit momentum and build the axisymmetric tangential winds and vorticity (Montgomery and Kallenbach 1997). In the current simulation, these likely VRW features are clearly present and also seen as enhanced PV filaments in Fig. 9a propagating outward between 15- and 25-km radius during hours 16–20. Given that these radii also correspond to the eventual secondary eyewall radius, these features possibly contribute to the SEF process, but the extent of this contribution is unclear. On the other hand, it is clear that the development of the secondary eyewall ramps up *only* when inward-propagating axisymmetric signals of enhanced vertical velocity (Fig. 1a) and PV (Fig. 9a) reach the radii of SEF. We argue that if VRWs had a greater, defining contribution to SEF in this simulation, then there would be a range of times when a secondary eyewall could ramp up, including at hour 20 or earlier hours when VRW are also active, depending on the storm's evolving vorticity radial profile. The SEF concurrence with the inward-propagating axisymmetric signal would then be largely coincidental. Instead, it is more likely that the timing and location of this axisymmetric signal is not a coincidence, and such an alignment with SEF suggests that the SBC has a larger, more defining contribution to SEF than VRWs *in this simulation*. Therefore, we focus the remainder of the current study on this feature.

b. PV budget during hours 19–20

The evolution of azimuthal mean PV and its tendency shown in Figs. 8 and 9 indicate that the eddy processes during hours 19 and 20 help shape the early systematic increase of the axisymmetric PV, which subsequently evolves into the outer eyewall. To further examine the dynamics that lead to the described PV changes, we now perform a more detailed PV budget analysis for these 2 h.

Figure 10 shows the actual and diagnosed changes of density-weighted PV during hours 19 and 20 h and the individual terms in Eq. (8). For simplicity, we group the $\overline{F_{q,\mathrm{mean}}}$ and $\overline{F_{q,\mathrm{eddy}}}$ terms into one single external forcing term $\overline{F_q}$. Consistent with Figs. 8e and 8f, the actual PV change (Fig. 10a) shows a broad area of increasing PV between 20- and 40-km radii, which is replicated reasonably well in the integrated PV change (Fig. 10b). We do note, however, that there are noticeable errors between the actual and integrated PV change within the boundary layer and near 3–4-km altitude and 40-km radius, possibly due to numerical integration error.

The PV flux convergence terms are shown in Figs. 10d–i, along with overlaid vectors that represent the total axisymmetric PV flux ($\overline{qu}$, $\overline{qw}$), and its mean ($\overline{q}\,\overline{u}$, $\overline{q}\,\overline{w}$) and eddy ($\overline{q'u'}$, $\overline{q'w'}$) components. Several important terms contribute to the PV enhancement near 20–40-km radius below z = 4 km. At $z < 1.5$ km, the dominant balance is between positive PV forcing (Fig. 10c) and vertical PV flux divergence (Fig. 10i), where strong vertical PV flux associated with convective updrafts carries the boundary layer PV upward. This results in flux divergence at $z < 1$ km that opposes the positive boundary layer PV forcing (due to surface sensible heat fluxes and frictional torque). Accompanying the intense convective updraft is radial PV flux convergence (Fig. 10f) at $z < 1.5$ km that helps shaping the overall PV increment in the boundary layer. The upward pointing PV fluxes, largely from eddy contributions (Fig. 10h), lead to vertical flux convergence at z = 2 km as they transport the boundary layer PV toward the free troposphere. This vertical flux convergence is partially countered by the negative PV forcing (due to the drop-off of sensible heat flux and friction across this altitude) and radial flux divergence, all of which shape the PV change at this level. The cancellation between the vertical PV flux convergence and PV forcing is the direct consequence of the impermeability theorem (Hayne and McIntyre 1987; Viúdez 1999), while radial flux convergence associated with boundary layer processes and the convective updraft shapes the local PV enhancement.

Above z = 2 km, prominent PV enhancements occur between 20- and 30-km and near 40-km radii (Fig. 10b). Both regions of positive tendency appear to result from PV forcing and radial flux convergence. As will be shown in later figures, stratiform precipitation processes are a major contributor to the positive PV forcing at these levels, where varying water phase changes produce the necessary vertical gradient of latent heating to generate midlevel PV (e.g., Franklin et al. 2006; Moon and Nolan 2010). This latent heating gradient is coupled with vertical mass flux divergence, which supports the vertical PV flux divergence at these levels. As a result, vertical PV flux divergence generally counteracts the positive PV forcing (Figs. 10c,f), which leaves radial flux convergence as a key contributor to the midlevel PV positive tendency, consistent with the impermeability theorem. Based on the

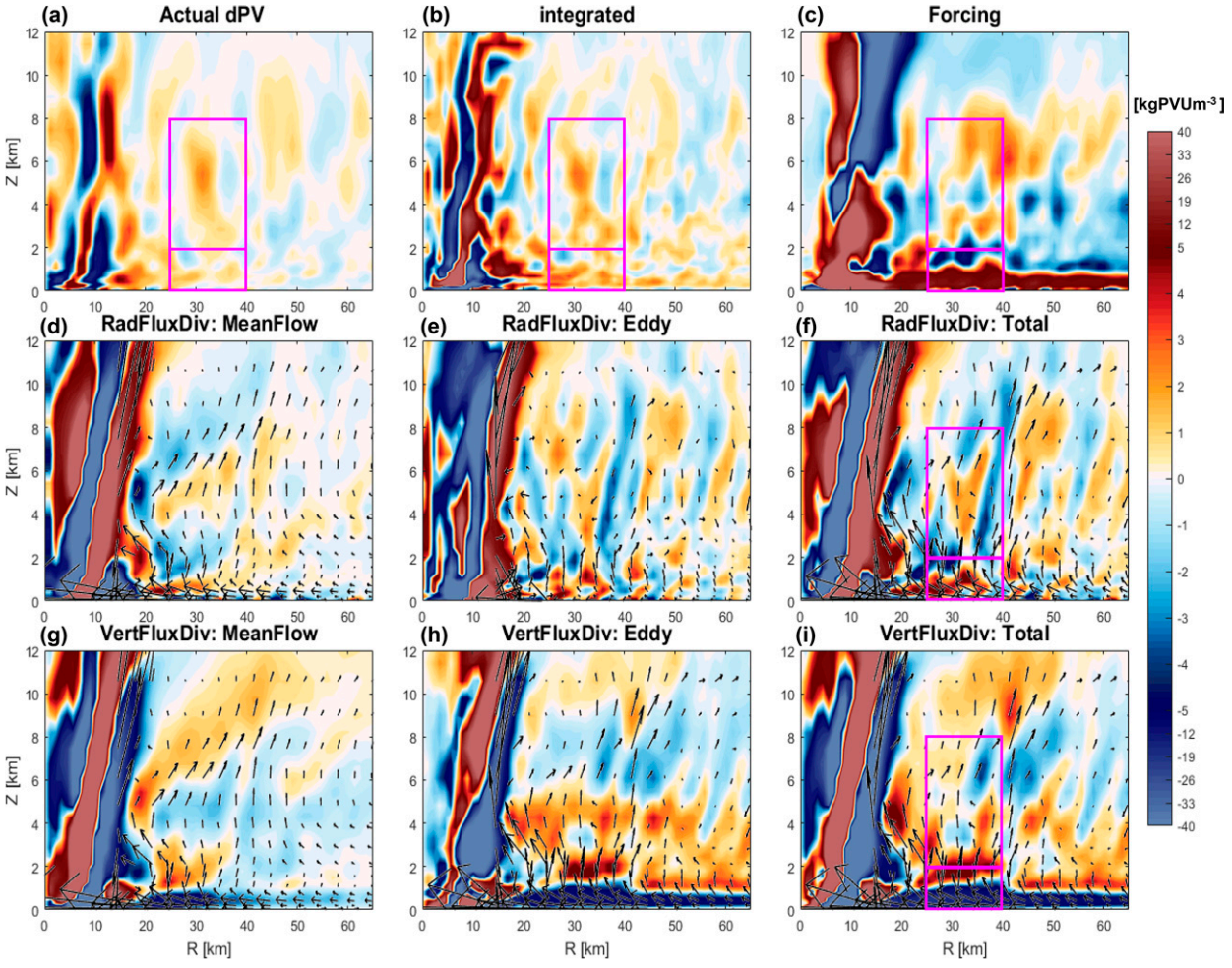

FIG. 10. Radius–height plots of the axisymmetric density-weighted PV (q) budget: (a) hourly changes in q during hours 19 and 20; (b) diagnosed hourly q changes; (c) external forcing $\overline{F_q}$; (d)–(f) radial flux convergence due to mean, eddy, and total PV fluxes; (g)–(i) vertical flux convergence due to mean, eddy, and total PV fluxes. Overlaid are corresponding vectors of mean, eddy, and total PV fluxes. The two magenta boxes in (b) highlight the regions of interest for Fig. 11.

flux vectors here, the total PV fluxes are emanating upward from the lower troposphere (Figs. 10d–f) at the rainband region. The radial convergence of these PV fluxes along with the locally generated PV then shape the structures of midlevel PV enhancement in Fig. 10b. One noteworthy point is that the mean flux convergence is generally weak outside of 20-km radius, and so the eddy flux convergence plays a larger role in the PV evolution during these hours, consistent with the finding shown in Fig. 9c. Overall, the enhancement of the outer PV maximum prior to SEF, both within the boundary layer and at midlevels, is primarily sourced from PV generated by asymmetric rainband processes, which is consistent with Judt and Chen (2010).

c. *Azimuthal–time evolution of the PV field and budget terms*

Given the importance of eddy processes in building the outer PV maximum, our next step is to determine the exact azimuthal locations of these eddy processes and their downwind evolution. To do this, the azimuthal–time evolution of the PV field and the budget terms are analyzed within the boundary layer ($z < 2$ km) and midtroposphere (between $z = 2$ and 8 km). With this goal, the density-weighted PV tendency is rewritten in the following form:

$$\frac{\partial q}{\partial t} = -\frac{1}{r}\frac{\partial r(\overline{q}\,\overline{u} + q'u')}{\partial r} - \frac{\partial(\overline{q}\,\overline{w} + q'w')}{\partial z} + F_q + \left[-\frac{1}{r}\frac{\partial r(\overline{q}u' + q'\overline{u})}{\partial r} - \frac{\partial(\overline{q}w' + q'\overline{w})}{\partial z} - \frac{1}{r}\frac{\partial qv}{\partial \lambda}\right], \quad (9)$$

where the first and second terms are the sum of the mean and eddy PV flux divergence in the radial and vertical directions, the third term is PV forcing, and the remaining terms in large parentheses include the asymmetric parts of the radial, vertical, and azimuthal PV flux divergence. Note that the terms in large parentheses vanish when taking the azimuthal mean of

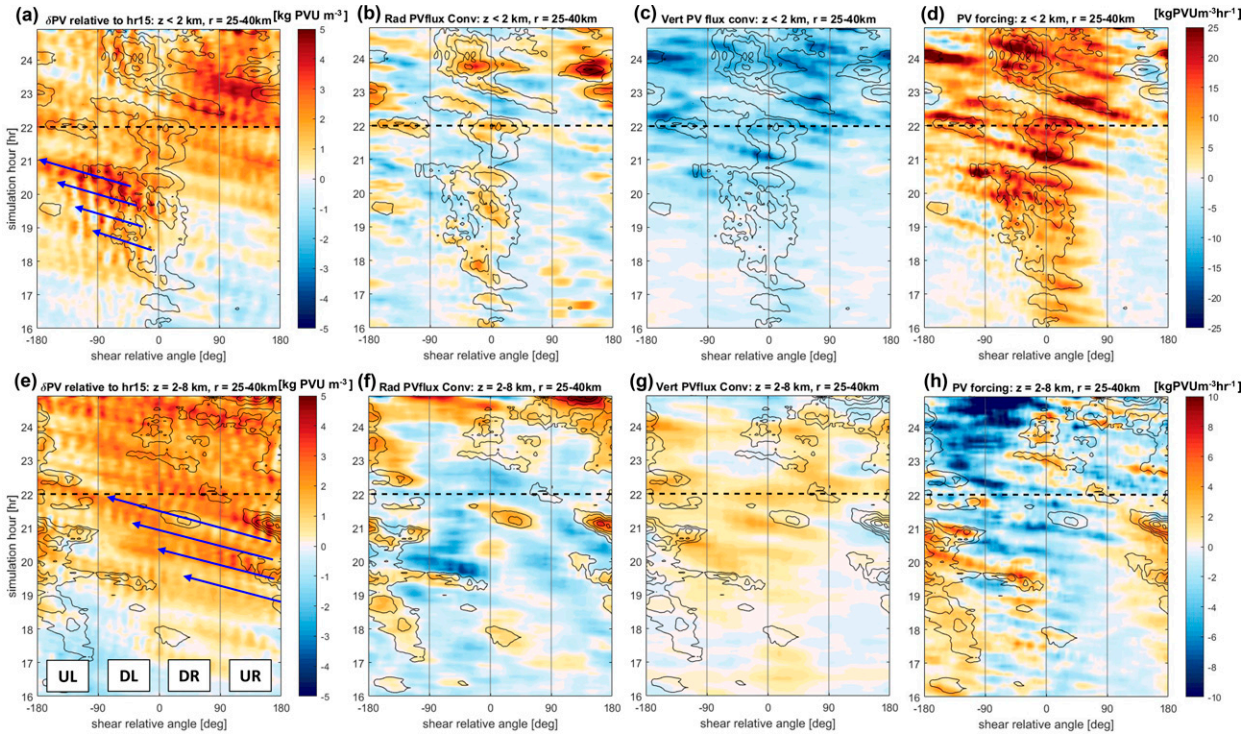

FIG. 11. Azimuthal–time evolution of (a),(e) density-weighted PV changes (δq) relative to hour 15 and budget terms averaged over the (top) low-level and (bottom) midlevel regions shown by the magenta boxes in Fig. 10. The remaining panels show the contributions from (b),(f) radial PV flux convergence, (c),(g) vertical PV flux convergence, and (d),(h) external forcing. Positive values of the net PV generation are contoured in black every 5 kg m^{-3} PVU h^{-1} in (a)–(d) and every 2 kg m^{-3} PVU h^{-1} in (e)–(h). The black dashed line indicates when the secondary eyewall becomes well established. Blue arrows highlight the downwind extension of PV from the region of positive net symmetric PV generation.

Eq. (9), indicating that these processes only redistribute the PV around the azimuthal circle, but do not produce net changes in azimuthal mean PV. Thus, these terms are neglected in this following analysis. On the other hand, the first three terms include all the processes that can contribute directly to the azimuthal mean PV; therefore, the azimuthal distribution of the sum of these terms represents the *source region* for the net azimuthal mean PV generation.

Figures 11a–d show the azimuth–time plots of PV changes relative to hour 15 and the first three terms in Eq. (9) averaged over the boundary layer box region in Fig. 10b (r = 25–40 km and $z < 2$ km). The black contours overlaid are the net azimuthal mean PV generation [the sum of the first three terms of Eq. (9)]. As shown in Fig. 11a, the left-of-shear boundary layer PV increases strongly between t = 17 and 21 h. During t = 19–21 h when the intense updraft zone emerges in the LS and UL quadrants, the PV increases are closely tied to the increase in net PV generation that lies slightly upwind and extends toward the UL quadrant; the newly generated PV then propagates downwind (as indicated by the blue arrows). Just later at 21.0 h, this strongest PV surge axisymmetrizes around all azimuths, helping to establish the secondary eyewall at t = 22 h (black dashed line) as defined by our vertical-velocity-based SEF timing and corroborated by the eddy/mean-flow analysis (Fig. 9c). Within the boundary layer, the PV generation is dominated by PV forcing (Fig. 11d), which includes sensible and latent heat fluxes from the ocean surface and boundary layer friction. Both PV generation and forcing signals share a similar structure and downwind extension toward the UL quadrant during t = 19–21 h. The vertical flux convergence (Fig. 11c) takes a similar structure as the PV forcing but with an opposite sign, indicating a net export of PV out of the boundary layer to above z = 2 km, consistent with Fig. 10i. Meanwhile, the radial PV flux convergence within the boundary layer (Fig. 11b) also has concurrent positive regions, but generally have minor contributions to the axisymmetric PV changes there.

Figures 11e–h show the same azimuth–time plots for the midtroposphere box region (r = 25–40 km and z = 2–8 km) shown in Fig. 10b. As shown in Fig. 11e, for times before t = 21 h, the midlevel net PV generation occurs in the UL and UR, which is downwind of the net PV generation in the DL quadrant boundary layer. This midlevel PV generation is mainly attributed to the PV forcing (Fig. 11h) and radial flux convergence (Fig. 11f) in the UL quadrant, which is cyclonically downwind from the low-level asymmetric updrafts left-of-shear at these times. This linkage is confirmed in Figs. 12a and 12b, which show the azimuth–height cross section (averaged between r = 25 and 40 km) and layer-mean plan view (z = 2–8 km) of the PV forcing,

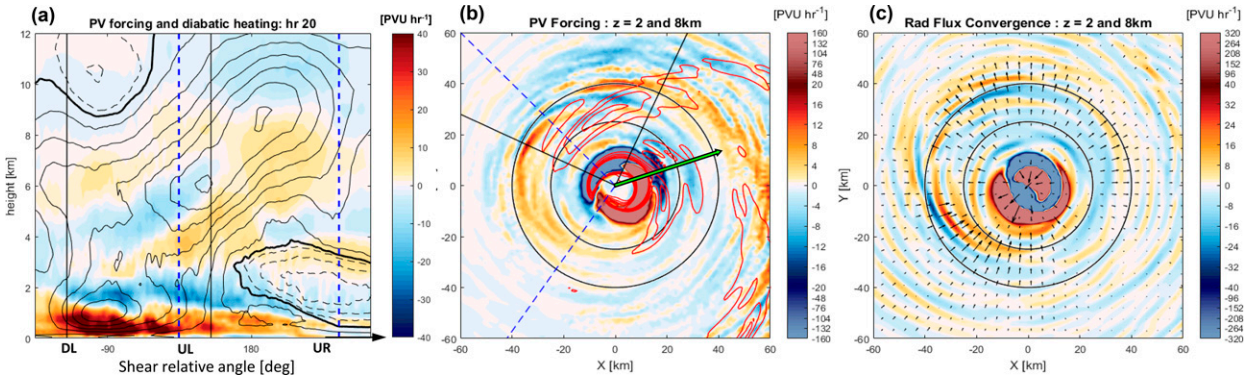

FIG. 12. (a) Azimuthal–height cross section of PV forcing F_q, radially averaged between $r = 25$ and 40 km at hour 20. Diabatic heating is contoured in solid black every 8×10^{-4} K s^{-1}, while cooling is contoured in dashed black at every 4×10^{-4} Ks^{-1}, with the zero contour thickened. The vertical black solid lines and vertical blue dashed lines indicate the azimuth ranges shown in (b). (b) Plan view of vertically averaged PV forcing F_q from $z = 2$ to 8 km. Upward velocity (averaged between $z = 0.5$ and 1.5 km) is contoured in red from 0.4 m s^{-1}. The black lines indicate the azimuth of the low-level updraft in the LS quadrant [as in (a)], while the blue dashed lines indicate the azimuth of the positive PV forcing F_q [as in (a)]. The black circles indicate $r = 25$- and 40-km radii. The green vector shows the direction of deep-layer environmental wind shear. (c) Plan view of vertically averaged radial PV flux convergence from $z = 2$ to 8 km. Vectors show the vertically averaged radial PV flux. The flux vectors at $r \leq 15$ km are scaled by 0.05 for visualization purposes.

diabatic heating (Fig. 12a) and low-level updraft (Fig. 12b) for hour 20. As convective updrafts are triggered in the left-of-shear quadrants and cyclonically propagate toward upshear quadrants (Figs. 12a,b), the diabatic heating structure gradually develops more stratiform-like characteristics, with diabatic heating and cooling above and below the melting level. Meanwhile, positive PV forcing occurs either underneath the diabatic heating maxima (in UL) or lies between heating and cooling (in the UR). This positive PV forcing signal is the same as that seen in Fig. 11h. As the net midlevel PV forcing inhabits the U.S. quadrants during 18–20 h, enhanced PV (Fig. 11e) propagates cyclonically downwind and extends into the UR and DR quadrants (as indicated by the blue arrows), and subsequently fills all quadrants at hour 21. We also note here that the filamentation time scale (Rozoff et al. 2006) of the LS asymmetric updraft during hour 20 is about 30–60 min (not shown), which is longer the typical 30-min lifespan of the individual convective elements in our simulation. This indicates that these updrafts are located in an environment dynamically favorable for their growth and cyclonic propagation around the storm. These times are in contrast with the filamentation times of about 15 min just radially inward of the updrafts; if these updrafts were initiated radially inward, then they would be sheared apart before reaching their greatest growth potential.

To understand the radial PV flux convergence shown in Figs. 11f and 10f more clearly, Fig. 12c shows the plan view of vertically averaged (between $z = 2$ and 8 km) radial PV flux convergence and the radial component of PV flux. From the plan view, we see that the radial PV flux convergence in the U.S. quadrant occurs slightly inward of the PV forcing (Fig. 12b), while divergence is covering part of the positive PV forcing region. Associated with this dipole pattern of PV flux convergence, the radial PV flux over this region is pointing inward, indicating that the PV generated by the local PV forcing is transported slightly inward by the PV flux. This radial PV flux convergence in the upshear quadrants is exactly the feature responsible for the radial PV convergence shown in Fig. 10e and 10f (as highlighted by the magenta box between $z = 2$ and 8 km). The relative placement between PV generation and PV shown in Figs. 11a, 11e, and 12a–c show that the PV axisymmetrized into the outer eyewall is associated with the asymmetric updraft and PV generation in the left-of-shear quadrants emerging at hours 19 and 20.

6. Conclusions

In this study, we examined the emergence and maintenance of an intense asymmetric updraft region and its impact on the evolution of potential vorticity prior to and during a secondary eyewall formation (SEF) event in a convection-permitting model simulation of Hurricane Matthew (2016), as a follow-on study to Yu et al. (2021). While Yu et al. examined the tangential wind evolution and dynamics associated with the rainband complex prior to SEF, this study focused on the persistent asymmetric low-level updrafts that developed within the left-of-shear stratiform rainband complex, which subsequently forged the onset of SEF. Specifically, we examined the role of the boundary layer θ_E asymmetries and surface cold pool in the triggering and maintenance of the low-level updrafts and we examined the resulting potential vorticity (PV) evolution that led to updraft axisymmetrization and the formation of a secondary eyewall.

The θ_E structures and a budget of the moist stability parameter $\partial\theta_E/\partial z$ were analyzed in the asymmetric updraft region of the SEF-precursor rainband in the left-of-shear (LS) quadrant. In the updraft core region, vertical advection of θ_E stabilizes the local atmosphere and is maintained at a strength that can consume the local moist instability on the time scale of 15 min, indicating the presence of a replenishment

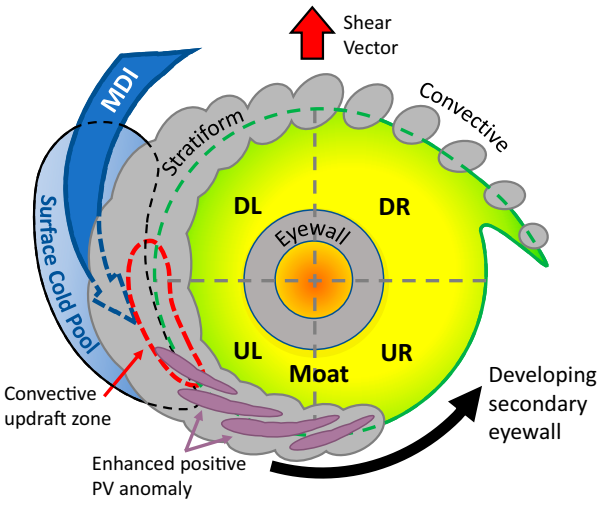

FIG. 13. A schematic diagram that illustrates the role of the stationary rainband complex in the SEF process. The gray and purple regions illustrate reflectivity of approximately 32 dBZ. The storm is oriented such that the shear vector is pointing north (red arrow). The mesoscale descending inflow (MDI; highlighted by the blue curved arrow) emerges at the left-of-shear regions, where the stationary rainband complex transitions from convective to stratiform precipitation. The surface cold pool (blue region) underneath the MDI interacts with the high-θ_E moist envelope (yellow region), resulting in a region with strong horizontal θ_E gradient (enclosed by red dashed line). Convective updraft is reinvigorated at this region, with the associated diabatic processes generate enhanced positive PV anomalies (highlighted by purple regions) that propagates cyclonically downwind and initiates the axisymmetrization of the outer eyewall.

mechanism of moist instability. Horizontal advection counters this stabilization by having warm-θ_E advection that decays with height near the top of the boundary layer. This differential warm-θ_E advection continuously destabilizes and replenishes the moist instability of the local atmosphere, maintaining the longevity of the strong updrafts.

Figure 13 shows a schematic diagram that illustrates the roles of the stationary rainband complex and the LS asymmetric updraft in the SEF process. This schematic is similar to the Fig. 17 of Didlake et al. (2018), but with a heavier emphasis on the sequence of processes at the LS updraft zone, which preconditions the SEF occurrence. This sequence of events begins at the LS rainband region, where a stream of mesoscale descending inflow (MDI; represented by the blue curved arrow) emerges in stratiform rainband precipitation in the DL quadrant, continuously flushing low-θ_E air into the TC boundary layer and establish a surface cold pool (blue shaded region), consistent with previous observational and modeling studies (Didlake and Houze 2013; Didlake et al. 2018; Qiu and Tan 2013; Chen 2018; Chen et al. 2018; Yu et al. 2021). As the inner edge of this LS surface cold pool interacts with the TC's inner-core envelope of high-θ_E air (yellow region), an azimuthal gradient of θ_E is established, which supports collocated long-lasting updrafts (as highlighted by the red dashed contour) in a manner consistent with previous modeling studies (Chen et al. 2018). Using a Lagrangian trajectory analysis, we also show that the development of the surface cold pool in the left-of-shear quadrants provides vertical lifting for the air parcels at its upwind, inner edge. The vertical lifting location relative to the cold pool and the updraft triggering mechanism are consistent with the buoyancy advection mechanism discussed in Yu and Didlake (2019).

Using a PV budget analysis, it is found that in this long-lasting LS updraft region, low-level PV is generated by boundary layer and convective diabatic processes, while the mid- and upper-level PV is generated by diabatic PV forcing, which has a diabatic heating structure consistent with precipitation fields that transition from convective to more stratiform characteristics. The cyclonic propagation and radial convergence of these different sources of PV (as highlighted by the purple regions in Fig. 13) systematically increases the azimuthal mean PV outside the primary eyewall prior to SEF. These low-level and midlevel processes occur in the span of 2 h and signals the establishment of the outer eyewall at hour 22.

The SEF pathway depicted herein contributes to the current understanding on SEF processes in the following ways. First, while consistent with previous studies highlighting the importance of PV generation in rainbands, our PV budget analysis further identifies that in sheared TCs, the rainband feature primarily responsible for the early enhanced PV generation is a low-level updraft region within the left-of-shear stratiform portion of the rainband complex. This enhanced updraft owes its existence to the interaction between a stratiform-cooling-driven surface cold pool and the high-θ_E inner core. Second, consistent with Wang et al. (2019), who highlighted enhanced eddy kinetic energy in the boundary layer prior to axisymmetrization, we note that the localized asymmetric PV forcing discussed herein results in a substantial increase in the eddy contribution to the azimuthal mean PV generation just prior to the SEF period.

The rainband processes analyzed in this study highlight a specific pathway for SEF from a stationary rainband complex in sheared TCs. Given that similar rainband diabatic forcing structures have been identified in numerous previous SEF studies in a quiescent environment (e.g., Qiu and Tan 2013; Wang et al. 2019), it would be important to further examine if the downwind rainband updrafts are generally maintained by a similar mechanism in those scenarios. Furthermore, one important unanswered question is how strong the asymmetric PV forcing needs to be to trigger the SEF axisymmetrization process. Finally, vortex Rossby waves propagating outward from the inner eyewall may also contribute to the maintenance of the asymmetric updraft and the development of the axisymmetric outer PV maximum, but the extent of the VRW contribution to SEF in our simulation remains unclear. Additional experiments and comparisons to observations are needed to investigate these outstanding issues.

Acknowledgments. We thank Kerry Emanuel, Kristen Corbosiero, Paul Markowski, and Steven Greybush for their valuable discussion and thoughtful comments on this study. We also thank the anonymous reviewers whose comments

led to significant improvements in the manuscript. This research was supported by the National Aeronautics and Space Administration under Grants NNX16AI21G (New Investigator Program), and by the National Science Foundation under Grants AGS-1810869 and AGS-1854607.

Data availability statement. The key variables of the model simulation analyzed in this study are openly available from the DataCommons@PSU at https://doi.org/10.26208/904n-0z74.

REFERENCES

Abarca, S. F., and M. T. Montgomery, 2013: Essential dynamics of secondary eyewall formation. *J. Atmos. Sci.*, **70**, 3216–3230, https://doi.org/10.1175/JAS-D-12-0318.1.

——, and ——, 2014: Departures from axisymmetric balance dynamics during secondary eyewall formation. *J. Atmos. Sci.*, **71**, 3723–3738, https://doi.org/10.1175/JAS-D-14-0018.1.

——, ——, and J. C. McWilliams, 2015: The azimuthally averaged boundary layer structure of a numerically simulated major hurricane. *J. Adv. Model. Earth Syst.*, **7**, 1207–1219, https://doi.org/10.1002/2015MS000457.

Bolton, D., 1980: The computation of equivalent potential temperature. *Mon. Wea. Rev.*, **108**, 1046–1053, https://doi.org/10.1175/1520-0493(1980)108<1046:TCOEPT>2.0.CO;2.

Chen, G., 2018: Secondary eyewall formation and concentric eyewall replacement in association with increased low-level inner-core diabatic cooling. *J. Atmos. Sci.*, **75**, 2659–2685, https://doi.org/10.1175/JAS-D-17-0207.1.

——, C. C. Wu, and Y. H. Huang, 2018: The role of near-core convective and stratiform heating/cooling in tropical cyclone structure and intensity. *J. Atmos. Sci.*, **75**, 297–326, https://doi.org/10.1175/JAS-D-17-0122.1.

Corbosiero, K. L., and J. Molinari, 2002: The effects of vertical wind shear on the distribution of convection in tropical cyclones. *Mon. Wea. Rev.*, **130**, 2110–2123, https://doi.org/10.1175/1520-0493(2002)130<2110:TEOVWS>2.0.CO;2.

——, and ——, 2003: The relationship between storm motion, vertical wind shear, and convective asymmetries in tropical cyclones. *J. Atmos. Sci.*, **60**, 366–376, https://doi.org/10.1175/1520-0469(2003)060<0366:TRBSMV>2.0.CO;2.

Dai, Y., S. J. Majumdar, and D. S. Nolan, 2017: Secondary eyewall formation in tropical cyclones by outflow–jet interaction. *J. Atmos. Sci.*, **74**, 1941–1958, https://doi.org/10.1175/JAS-D-16-0322.1.

Didlake, A. C., and R. A. Houze Jr., 2013: Dynamics of the stratiform sector of a tropical cyclone rainband. *J. Atmos. Sci.*, **70**, 1891–1911, https://doi.org/10.1175/JAS-D-12-0245.1.

——, P. D. Reasor, R. F. Rogers, and W. C. Lee, 2018: Dynamics of the transition from spiral rainbands to a secondary eyewall in Hurricane Earl (2010). *J. Atmos. Sci.*, **75**, 2909–2929, https://doi.org/10.1175/JAS-D-17-0348.1.

Fang, J., and F. Zhang, 2012: Effect of beta shear on simulated tropical cyclones. *Mon. Wea. Rev.*, **140**, 3327–3346, https://doi.org/10.1175/MWR-D-10-05021.1.

Franklin, C. N., G. J. Holland, and P. T. May, 2006: Mechanisms for the generation of mesoscale vorticity features in tropical cyclone rainbands. *Mon. Wea. Rev.*, **134**, 2649–2669, https://doi.org/10.1175/MWR3222.1.

Gamache, J. F., F. D. Marks, and F. Roux, 1995: Comparison of three airborne Doppler sampling techniques with airborne in situ wind observations in Hurricane Gustav (1990). *J. Atmos. Oceanic Technol.*, **12**, 171–181, https://doi.org/10.1175/1520-0426(1995)012<0171:COTADS>2.0.CO;2.

Hausman, S. A., K. V. Ooyama, and W. H. Schubert, 2006: Potential vorticity structure of simulated hurricanes. *J. Atmos. Sci.*, **63**, 87–108, https://doi.org/10.1175/JAS3601.1.

Hawkins, H., and S. M. Imbembo, 1976: The structure of a small, intense hurricane—Inez 1966. *Mon. Wea. Rev.*, **104**, 418–442, https://doi.org/10.1175/1520-0493(1976)104<0418:TSOASI>2.0.CO;2.

Haynes, P. H., and M. McIntyre, 1990: On the conservation and impermeability theorems for potential vorticity. *J. Atmos. Sci.*, **47**, 2021–2031, https://doi.org/10.1175/1520-0469(1990)047<2021:OTCAIT>2.0.CO;2.

Hong, S. Y., J. Dudhia, and S. H. Chen, 2004: A revised approach to ice microphysical processes for the bulk parameterization of clouds and precipitation. *Mon. Wea. Rev.*, **132**, 103–120, https://doi.org/10.1175/1520-0493(2004)132<0103:ARATIM>2.0.CO;2.

Huang, Y. H., M. T. Montgomery, and C. C. Wu, 2012: Concentric eyewall formation in Typhoon Sinlaku (2008). Part II: Axisymmetric dynamical processes. *J. Atmos. Sci.*, **69**, 662–674, https://doi.org/10.1175/JAS-D-11-0114.1.

Judt, F., and S. S. Chen, 2010: Convectively generated potential vorticity in rainbands and formation of the secondary eyewall in Hurricane Rita of 2005. *J. Atmos. Sci.*, **67**, 3581–3599, https://doi.org/10.1175/2010JAS3471.1.

Kepert, J., 2013: How does the boundary layer contribute to eyewall replacement cycles in axisymmetric tropical cyclones? *J. Atmos. Sci.*, **70**, 2808–2830, https://doi.org/10.1175/JAS-D-13-046.1.

——, and D. S. Nolan, 2014: Reply to "Comments on 'How does the boundary layer contribute to eyewall replacement cycles in axisymmetric tropical cyclones?'" *J. Atmos. Sci.*, **71**, 4692–4704, https://doi.org/10.1175/JAS-D-14-0014.1.

Li, Q., and Y. Wang, 2012: Formation and quasi-periodic behavior of outer spiral rainbands in a numerically simulated tropical cyclone. *J. Atmos. Sci.*, **69**, 997–1020, https://doi.org/10.1175/2011JAS3690.1.

——, ——, and Y. Duan, 2014: Effects of diabatic heating and cooling in the rapid filamentation zone on structure and intensity of a simulated tropical cyclone. *J. Atmos. Sci.*, **71**, 3144–3163, https://doi.org/10.1175/JAS-D-13-0312.1.

——, ——, and ——, 2017: A numerical study of outer rainband formation in a sheared tropical cyclone. *J. Atmos. Sci.*, **74**, 203–227, https://doi.org/10.1175/JAS-D-16-0123.1.

Martinez, J., M. M. Bell, R. F. Rogers, and J. D. Doyle, 2019: Axisymmetric potential vorticity evolution of Hurricane Patricia (2015). *J. Atmos. Sci.*, **76**, 2043–2063, https://doi.org/10.1175/JAS-D-18-0373.1.

Miyamoto, Y., and T. Takemi, 2013: A transition mechanism for the axisymmetric spontaneous intensification of tropical cyclones. *J. Atmos. Sci.*, **70**, 112–129, https://doi.org/10.1175/JAS-D-11-0285.1.

——, D. S. Nolan, and N. Sugimoto, 2018: A dynamical mechanism for secondary eyewall formation in tropical cyclones. *J. Atmos. Sci.*, **75**, 3965–3986, https://doi.org/10.1175/JAS-D-18-0042.1.

Montgomery, M. T., and R. J. Kallenbach, 1997: A theory for vortex Rossby-waves and its application to spiral bands and intensity changes in hurricanes. *Quart. J. Roy. Meteor. Soc.*, **123**, 435–465, https://doi.org/10.1002/qj.49712353810.

Moon, Y., and D. S. Nolan, 2010: The dynamic response of the hurricane wind field to spiral rainband heating. *J. Atmos. Sci.*, **67**, 1779–1805, https://doi.org/10.1175/2010JAS3171.1.

Noh, Y., W. G. Cheon, S. Y. Hong, and S. Raasch, 2003: Improvement of the K-profile model for the planetary boundary layer based on large eddy simulation data. *Bound.-Layer Meteor.*, **107**, 401–427, https://doi.org/10.1023/A:1022146015946.

Nystrom, R. G., F. Zhang, E. B. Munsell, S. A. Braun, J. A. Sippel, Y. Weng, and K. Emanuel, 2018: Predictability and dynamics of Hurricane Joaquin (2015) explored through convection-permitting ensemble sensitivity experiments. *J. Atmos. Sci.*, **75**, 401–424, https://doi.org/10.1175/JAS-D-17-0137.1.

Qiu, X., and Z. M. Tan, 2013: The roles of asymmetric inflow forcing induced by outer rainbands in tropical cyclone secondary eyewall formation. *J. Atmos. Sci.*, **70**, 953–974, https://doi.org/10.1175/JAS-D-12-084.1.

Riemer, M., 2016: Meso-β-scale environment for the stationary band complex of vertically sheared tropical cyclones. *Quart. J. Roy. Meteor. Soc.*, **142**, 2442–2451, https://doi.org/10.1002/qj.2837.

——, and M. T. Montgomery, 2011: Simple kinematic models for the environmental interaction of tropical cyclones in vertical wind shear. *Atmos. Chem. Phys.*, **11**, 9395–9414, https://doi.org/10.5194/acp-11-9395-2011.

——, ——, and M. E. Nicholls, 2013: Further examination of the thermodynamic modification of the inflow layer of tropical cyclones by vertical wind shear. *Atmos. Chem. Phys.*, **13**, 327–346, https://doi.org/10.5194/acp-13-327-2013.

Rotunno, R., and K. A. Emanuel, 1987: An air–sea interaction theory for tropical cyclones. Part II: Evolutionary study using a nonhydrostatic axisymmetric numerical model. *J. Atmos. Sci.*, **44**, 542–561, https://doi.org/10.1175/1520-0469(1987)044<0542:AAITFT>2.0.CO;2.

Rozoff, C. M., W. H. Schubert, B. D. McNoldy, and J. P. Kossin, 2006: Rapid filamentation zones in intense tropical cyclones. *J. Atmos. Sci.*, **63**, 325–340, https://doi.org/10.1175/JAS3595.1.

Schubert, W. H., and J. J. Hack, 1983: Transformed Eliassen balanced vortex model. *J. Atmos. Sci.*, **40**, 1571–1583, https://doi.org/10.1175/1520-0469(1983)040<1571:TEBVM>2.0.CO;2.

——, S. A. Hausman, and M. Garcia, 2001: Potential vorticity in a moist atmosphere. *J. Atmos. Sci.*, **58**, 3148–3157, https://doi.org/10.1175/1520-0469(2001)058<3148:PVIAMA>2.0.CO;2.

Skamarock, W. C., and Coauthors, 2008: A description of the Advanced Research WRF version 3. NCAR Tech. Note NCAR/TN-475+STR, 113 pp., http://dx.doi.org/10.5065/D68S4MVH.

Smith, R. K., M. T. Montgomery, and H. Zhu, 2005: Buoyancy in tropical cyclones and other rapidly rotating atmospheric vortices. *Dyn. Atmos. Oceans*, **40**, 189–208, https://doi.org/10.1016/j.dynatmoce.2005.03.003.

Sprenger, M., and H. Wernli, 2015: The LAGRANTO Lagrangian analysis tool—Version 2.0. *Geosci. Model Dev.*, **8**, 2569–2586, https://doi.org/10.5194/gmd-8-2569-2015.

Terwey, W. D., and M. T. Montgomery, 2008: Secondary eyewall formation in two idealized, full-physics modeled hurricanes. *J. Geophys. Res.*, **113**, D12112, https://doi.org/10.1029/2007JD008897.

Tyner, B., P. Zhu, J. A. Zhang, S. Gopalakrishnan, F. Marks, and V. Tallapragada, 2018: A top-down pathway to secondary eyewall formation in simulated tropical cyclones. *J. Geophys. Res. Atmos.*, **123**, 174–197, https://doi.org/10.1002/2017JD027410.

Viúdez, A., 1999: On Ertel's potential vorticity theorem. On the impermeability theorem of potential vorticity. *J. Atmos. Sci.*, **56**, 507–516, https://doi.org/10.1175/1520-0469(1999)056<0507:OESPVT>2.0.CO;2.

Wang, H., Y. Wang, J. Xu, and Y. Duan, 2019: The axisymmetric and asymmetric aspects of the secondary eyewall formation in a numerically simulated tropical cyclone under idealized conditions on an *f* plane. *J. Atmos. Sci.*, **76**, 357–378, https://doi.org/10.1175/JAS-D-18-0130.1.

Wang, Y. F., and Z. M. Tan, 2020: Outer rainbands-driven secondary eyewall formation of tropical cyclones. *J. Atmos. Sci.*, **77**, 2217–2236, https://doi.org/10.1175/JAS-D-19-0304.1.

Weng, Y., and F. Zhang, 2012: Assimilating airborne Doppler radar observations with an ensemble Kalman filter for convection-permitting hurricane initialization and prediction: Katrina (2005). *Mon. Wea. Rev.*, **140**, 841–859, https://doi.org/10.1175/2011MWR3602.1.

——, and ——, 2016: Advances in convection-permitting tropical cyclone analysis and prediction through EnKF assimilation of reconnaissance aircraft observations. *J. Meteor. Soc. Japan*, **94**, 345–358, https://doi.org/10.2151/jmsj.2016-018.

Wernli, B. H., and H. C. Davies, 1997: A Lagrangian-based analysis of extratropical cyclones. I: The method and some applications. *Quart. J. Roy. Meteor. Soc.*, **123**, 467–489, https://doi.org/10.1002/qj.49712353811.

Willoughby, H. E., F. D. Marks, and R. H. Feinberg, 1984: Stationary and moving convective bands in hurricanes. *J. Atmos. Sci.*, **41**, 3189–3211, https://doi.org/10.1175/1520-0469(1984)041<3189:SAMCBI>2.0.CO;2.

Yu, C.-L., and A. C. Didlake, 2019: Impact of stratiform rainband heating on the tropical cyclone wind field in idealized simulations. *J. Atmos. Sci.*, **76**, 2443–2462, https://doi.org/10.1175/JAS-D-18-0335.1.

——, ——, F. Zhang, and R. G. Nystrom, 2021: Asymmetric rainband processes leading to secondary eyewall formation in a model simulation of Hurricane Matthew. *J. Atmos. Sci.*, **78**, 29–49, https://doi.org/10.1175/JAS-D-20-0061.1.

Zhang, F., and Y. Weng, 2015: Predicting hurricane intensity and associated hazards: A five-year real-time forecast experiment with assimilation of airborne Doppler radar observations. *Bull. Amer. Meteor. Soc.*, **96**, 25–33, https://doi.org/10.1175/BAMS-D-13-00231.1.

——, D. Tao, Y. Q. Sun, and J. D. Kepert, 2017: Dynamics and predictability of secondary eyewall formation in sheared tropical cyclones. *J. Adv. Model. Earth Syst.*, **9**, 89–112, https://doi.org/10.1002/2016MS000729.

Zhu, P., and Coauthors, 2015: Impact of subgrid-scale processes on eyewall replacement cycle of tropical cyclones in HWRF system. *Geophys. Res. Lett.*, **42**, 10 027–10 036, https://doi.org/10.1002/2015GL066436.